Computational Mechanics
https://doi.org/10.1007/s00466-024-02555-4

ORIGINAL PAPER

Simulation of drill-string systems with fluid–structure and contact interactions in realistic geometries

Sara Galasso[1] · Luca Santelli[2] · Raffaello Zambetti[3] · Giulio G. Giusteri[1]

Received: 1 February 2024 / Accepted: 12 September 2024

Abstract
We propose a method for the simulation of the nonlinear dynamics of drill-string systems and the assessment of the stresses to which the pipe is subject under realistic conditions in drilling operations. The formulation of the evolution equations of the drill-string is based on the special Euclidean strand equations for the stresses and momenta of geometrically exact viscoelastic rods. For the spatial discretisation, we employ a finite-difference method on a staggered grid and the time integration is based on an adaptive Runge–Kutta method. The model allows to simulate the nonlinear dissipative dynamics of rods, with realistic material parameters, confined inside tubular wells of arbitrary shape, accounting for fluid–structure and contact interactions. The comparison of the numerical results with field data collected in drilling operations shows the effectiveness of our method in reproducing the mechanical response of real drill-string systems and the robustness in providing accurate predictions when tested in computationally-challenging settings.

Keywords Drill-string system · Viscoelastic Cosserat rod · Contact interaction · Fluid–structure interaction · Constrained buckling

1 Introduction

In the oil and gas industry, mathematical and numerical models have played a crucial role since the 1980 s, with the early works of Johansick et al. [1], Locke [2], and Maidla and Wojtanowicz [3]. Indeed, the capability of evaluating the time and space evolution of physical quantities through the solution of governing equations can effectively complement the information measured on fields.

Drilling operations are performed using a drill-bit, which fractures the rock formation to dig a downhole until the reservoir level. Tubular pipes of different sizes with a telescopic configuration connect the drill-bit to the rig at the surface and constitute the *drill-string*. Drilling mud, used to cool and lubricate the drill bit and transport the rock cuttings, is pumped inside the drill pipe and flows back to the surface in the annulus between the drill pipe and the borehole. A description of how drill-string systems work is detailed in Baker [4].

Motivated by practical requirements, such as optimising the rate of penetration (that is the speed at which the well is being drilled), while securing the structural integrity and fatigue life of the tools [5], mathematical and numerical models are called for providing reliable and efficient predictions, so to test stress limits and prevent failures. For example, understanding loads on tubular components has a significant role, as a better definition of loads reduces uncertainties, which otherwise shall be managed by higher design safety factors with an increase of costs and in some extreme cases may deem the well unfeasible [6]. Currently, on the market, there is no specific software for drill-string dynamics

Sara Galasso and Luca Santelli are contributed equally to this work.

✉ Giulio G. Giusteri
giulio.giusteri@unipd.it

Sara Galasso
sara.galasso@unipd.it

Luca Santelli
lsantelli@bcamath.org

Raffaello Zambetti
rzambetti@tenaris.com

[1] Department of Mathematics "Tullio Levi-Civita", Università degli Studi di Padova, Via Trieste 63, Padova 35121, Italy

[2] CFD Modelling and Simulation, Basque Center for Applied Mathematics, Alameda de Mazarredo 14, Bilbao 48009, Basque Country, Spain

[3] Tenaris, Piazza Caduti 6 Luglio 1944 1, Dalmine 24044, Italy

Published online: 27 December 2024

and general-purpose finite elements software can solve only a limited amount of problems, such as simple trajectories and limited contacts. However, in recent years, the industry started approaching more complex physical and mathematical models, as well as advanced numerical methods, and challenging the limitations of the existing ones, as discussed in Mitchell and Samuel [7]. In particular, the greatest challenges come from describing the dynamical response of the drill-string during the drilling process. Indeed, on the one hand, working with a very slender and flexible structure (the length of the drill-string has the order of kilometres), it is important to capture the intrinsic nonlinearities of the system, and, on the other, abrupt and intense events like collisions or sudden release of energy, which may overload the string and lead to failure, require to investigate the details of the drill-string–wellbore interactions.

A family of well-known models consists of Torque and Drag models. They describe the interaction of the drill-string with the wellbore as a result of forces, such as friction, buoyancy, and viscosity, acting longitudinally and tangentially. In particular, friction factors are adopted to match field data as presented in [8] and [9]. The friction factors not only include friction effects, but also other factors that may impact torque and drag forces such as hole tortuosity, hole cleanness, and all other physical factors that are difficult to define and model, such as mud lubrication and drill-string-rock interaction. Torque and Drag models can be divided into two different approaches: Soft String, where the string is considered continuously in contact with the wellbore and has no bending stiffness, like a chain model, and Stiff String, based on a more sophisticated model, typically Euler and Timoshenko rod theory, which take into account the rod stiffness and the borehole clearance. A comprehensive comparison between the two models can be found in the work of Mirhaj et al. [10]. Nonetheless, up to date, both approaches consider only the static geometric configuration of the drill-string, and lack therefore in capturing dynamic phenomena, such as vibrations, impact between the string and the wellbore, and stick–slip. As a matter of fact, dynamic loads can play a significant role in the fatigue life of the drill-string, as described in [11–14]. Accordingly, in most recent years, several approaches to perform analyses in the time domain are appearing [15], though they are mainly limited to short drill-strings [16] or to specific applications [17]. Modal analysis revealed to be useful in some cases [18–20], however, it is not representative of real operations: one of the main reasons is the continuously changing contact points between the tubular and the well, which would require a specific modal analysis for each configuration. Besides, dynamic effects in vibrations analyses are often uncoupled: focusing on individual vibrations, such as axial, torsional or bending [21–23], or partial coupling between longitudinal/torsional, longitudinal/lateral, or lateral/torsional [11, 24–27]. More complex methods allow a fully coupled description, however, in these analyses, the geometry of the well is simplified [28–30].

In this work, we propose an innovative approach for a dynamic model of drill-string systems in realistic geometries. The description relies on the formulation of the nonlinear dynamics of one-dimensional geometrically exact rods in a three-dimensional space based on the dynamics of special Euclidean strands [31]. While the geometric nonlinearities of the system intrinsically couple the axial, torsional, and lateral degrees of freedom, this approach has the advantage that the evolution equations are given in terms of variables which are defined on a linear space. The local nature of the representation favours a flexible implementation of external forces and boundary conditions, and avoids shear locking effects. An analysis of the accuracy of the spatial discretisation method against benchmark solutions is provided in Ref. [31].

We consider the constrained dynamics of drill-strings within wellbores which we allow to have arbitrary tubular configurations. Geometric deformations introduce, in particular, nontrivial dynamic loads due to impacts with the well. We provide an accurate and efficient scheme for the contact interactions, accounting for longitudinal and tangential friction. The interaction of the drill-bit with the bottom of the wellbore is modelled respecting field evidence, which indicates a linear coupling between the compressive load and the torque produced by friction. Furthermore, we enrich the realism of the model with the inclusion of dissipative contributions due to the hydrodynamic interaction with drilling fluids, which account not only for the velocity but also for the position of the rod relative to the well. This is achieved by implementing the translating–rotating model proposed by Finn and Cox [32] and adjusting the values of effective coefficients.

Overall, we provide a tool to study the nonlinear dynamics of drill-strings, in very general drilling configurations and with computationally efficient performances. In fact, from the numerical simulations that we present, the method shows a great capability of reproducing the nonlinear dynamics of drill-strings over several minutes in realistic operating conditions, with a satisfactory agreement with field data. The method that we present in this work can be of interest also for different applications in which slender objects undergo significant deformations in domains that present geometrical constraints. One could indeed present in a less special context our techniques. Nevertheless, it seems important to give a coherent account of the results in the special application that motivated our research.

The article is organised as follows. We detail the computational method we developed in Sect. 2: first, we recall the setting for geometrically exact viscoelastic rods described in terms of Lie algebraic quantities, followed by the discretisation scheme adopted for the numerical integration of

the evolution equations, which consists of a finite-difference scheme on a staggered grid and an explicit Runge–Kutta 5(4) time integration with adaptive time stepping; and then, we present the model for the fluid–structure and contact interactions. Section 3 deals with the phenomenon of buckling under compressive loads at the bit, in the absence and presence of the confining well. In the former case, a linear stability analysis of the spatially discretised rod allows us to determine, in a numerically efficient way, the values of critical loads for both weightless and heavy rods. Constrained post-buckling configurations are then discussed, proving the effectiveness of our method in the nonlinear large-displacement static regime. In Sect. 4, we present numerical studies for the dynamics of various drill-string systems in realistic geometries. We test the results of the simulations against real data collected in drilling operations, showing that it succeeds in reproducing the time evolution of physical quantities measured at the surface. The method proved to be robust even in computationally-challenging configurations, such as very long rods inside wells having tortuous trajectories, in which contacts and loads have a significant impact on the dynamics of the drill-string.

2 The computational method

We propose a method for the simulation of the dynamics of drill-string systems and the assessment of the stresses to which the pipe is subject under realistic conditions in drilling operations. We build the evolution equations of the drill-strings on the computational model proposed by Giusteri et al. [31], which provides a description of the nonlinear dynamics of viscoelastic rods. The formulation is based on the $SE(3)$-strand equation for the stresses and momenta, with a finite-difference discretisation method on a staggered grid and adaptive time-stepping integration. We assume the rod to have circular cross sections, while no limitations on its relaxed shape are imposed. We provide a description for the contact interactions between the rod and the well and account for dissipation due to the drilling fluids present inside the wellbore.

2.1 The evolution equations

In [31], a geometrically exact description for the dynamics of slender structures is provided by exploiting the Lie group structure of the configuration space of Cosserat rods, namely the special Euclidean group $SE(3)$, and by understanding the generalised velocities of rigid cross sections and generalised strains of the rod as elements of the associated Lie algebra $\mathfrak{se}(3)$. Therein, following this approach, the evolution equations for a viscoelastic Cosserat rod are derived in terms of the variables associated with the corresponding momenta and stresses. A finite-difference spatial discretisation is hence introduced on a staggered grid, while the time integration is performed with a semi-implicit method. Such a computational scheme is particularly flexible as it exploits the local nature of the representation and accounts intrinsically for nonlinear effects, and was proven to ensure a good computational performance. These aspects are particularly useful for capturing the dynamics of pipes in drilling processes, where geometric nonlinearities, external forces, and dissipative effects must be accounted for. We will rely on the dynamic equations therein derived, but, while we adopt the aforementioned spatial discretisation, we will use for the time integration an explicit Runge–Kutta method with adaptive stepsize, which revealed to be more suited to our problem.

2.1.1 Equations for a viscoelastic rod

We briefly recall the formulation of Giusteri et al. [31]. The mechanical structure under consideration is modelled as a special Cosserat rod, whose elastic response is linear in the strains (with respect to the preferred ones) and the different components are not coupled. Internal and external viscous dissipation is then added to the system.

In the same notation as [31], each rigid cross section of the rod is identified by the position $\boldsymbol{x}$ of its centre of mass and a reference basis $(\boldsymbol{d}_1, \boldsymbol{d}_2, \boldsymbol{d}_3)$, where the three versors are taken aligned with the principal axes of inertia of the cross section, with $\boldsymbol{d}_3$ orthogonal to the cross-sectional plane. The corresponding velocity vector is denoted by $\dot{\boldsymbol{x}}$, while $\boldsymbol{\omega}$ represents its angular velocity vector. At each time $t \in [0, +\infty)$, the configuration of the rod is parametrised by $s \in [0, L]$, with L denoting its reference length. The evolution of the rod is described in terms of the momentum and stress fields, which are represented by the six-component vectors P and Σ. Specifically, the field P represents the linear density of angular and linear momenta along $\boldsymbol{d}_3, \boldsymbol{d}_1, \boldsymbol{d}_2$, while Σ collects internal torques and forces of the rod and its components are the stresses associated with twist, curvatures, stretching and shearings, respectively. Both P and Σ are elements of the dual of the special Euclidean algebra, $\mathfrak{se}(3)^* \cong \mathfrak{se}(3)$; as functions of (s, t), their differentiation in space and time is denoted, respectively, by a prime and a superimposed dot. The momentum P is dual to the vector V of generalised velocities and Σ is dual to the vector of strains U through the relations

$$P = \mathbb{M}V \quad \text{and} \quad \Sigma = \mathbb{A}(U - \bar{U}),$$

where the (6×6)-matrices $\mathbb{M}$ and $\mathbb{A}$ denote, respectively, the elastic stiffness and rigid-body inertia at each rigid cross section of the rod and $\bar{U}$ is the preferred strain state that corresponds to vanishing elastic stresses. Even though in our examples we always consider straight stress-free configu-

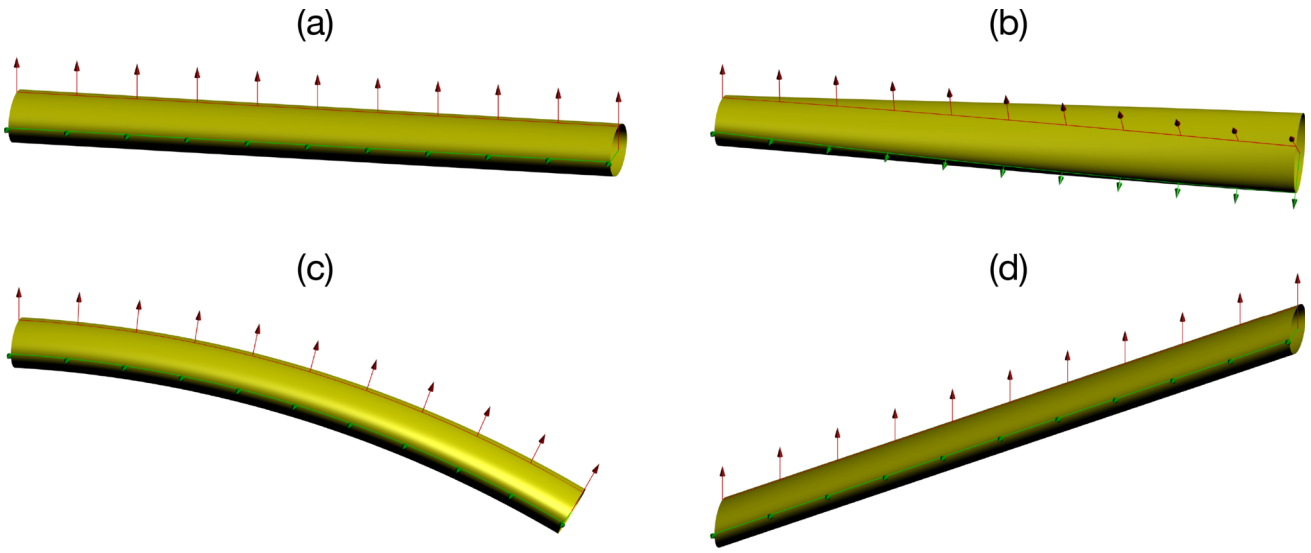

Fig. 1 The degrees of freedom encoded in the strain vector U represent uniform deformations of each rod segment. A straight rod segment (**a**) corresponds to $U = (0, 0, 0, 1, 0, 0)$ with the sole stretching component different from zero, a non-vanishing U_1 activates twisting (**b**), while the components U_2 and U_3 are responsible for bending in orthogonal directions (**c**), and U_5 and U_6 encode shearing of adjacent cross section (**d**)

rations, the method can accommodate arbitrary stress-free shapes with appropriate choices of the components of $\bar{U}$. More specifically, the strain component U_1 activates twisting deformations, U_2 and U_3 are associated with bending modes in two orthogonal directions, U_4 describes the axial stretching of the rod, while U_5 and U_6 measure the shearing of adjacent cross sections in two orthogonal directions (Fig. 1). For instance, a straight rod is characterised by the uniform strain vector $U = (0, 0, 0, 1, 0, 0)$.

We can derive from a variational principle the Euler-Poincaré equations in (P, Σ), for the conservative system, and complement them with a suitable compatibility condition. The resulting equations are a closed system of PDEs written in terms of the adjoint operator $\mathrm{ad}_X(Y) := XY - YX$ and its dual $\mathrm{ad}^{\mathsf{T}}_X(Z) \cdot Y := Z \cdot \mathrm{ad}_X(Y)$, for any $X, Y \in \mathfrak{se}(3)$ and $Z \in \mathfrak{se}(3)^*$. Dissipation is then included in the system by adding a term proportional to the generalised velocities, which accounts for external viscous drag, and a term linearly dependent on the time derivative of the strains, which models internal dissipation. Consequently, the evolution equations for the dynamics of the viscoelastic rod read

$$\begin{aligned} \dot{P} - \Sigma' = {} & \mathrm{ad}^{\mathsf{T}}_{\mathbb{M}^{-1}P} P - \mathrm{ad}^{\mathsf{T}}_{\mathbb{A}^{-1}\Sigma+\bar{U}} \Sigma \\ & - \mathbb{D}_{\mathrm{ex}} \mathbb{M}^{-1} P - \mathbb{D}_{\mathrm{in}} \mathbb{A}^{-1} \dot{\Sigma} + F \end{aligned} \tag{1}$$

$$\dot{\Sigma} - \mathbb{A}(\mathbb{M}^{-1}P)' = \mathbb{A}\,\mathrm{ad}_{\mathbb{A}^{-1}\Sigma+\bar{U}}(\mathbb{M}^{-1}P) \tag{2}$$

where $\mathbb{D}_{\mathrm{ex}}$ and $\mathbb{D}_{\mathrm{in}}$ are the dissipation matrices associated with external drag and internal mechanical dissipation, respectively, while F represents external torque and force densities acting on each rigid cross section. The evolution equations are finally complemented with the desired boundary conditions. We choose to assign a prescribed motion $\bar{P}_0(t)$ at the head of the rod and a given stress $\bar{\Sigma}_{\mathrm{e}}(t)$ at the bit, namely,

$$P(0, t) = \bar{P}_0(t), \qquad \Sigma(L, t) = \bar{\Sigma}_{\mathrm{e}}(t). \tag{3}$$

Note that in our setting the variable fields take values in the Lie algebra associated with rigid body motions. This approach is somewhat complementary to other techniques that directly discretise the degrees of freedom in the Lie group such as those based on isogeometric collocation methods [33–35].

2.1.2 Discretisation scheme

We adopt the spatial discretisation of the evolution equations (1)–(2) developed by Giusteri et al. [31], which relies on a finite-difference approximation designed to respect the nature of the variables used in the description. Specifically, the peculiarity of the method is that, having partitioned the spatial interval $[0, L]$ into $0 = s_0 \leq s_1 \leq \cdots \leq s_N = L$, with N the number of segments, the discretised variables are assigned on a staggered grid, which has the following structure (see Fig. 2). The momenta (and velocities) take value on the nodes of the partition and are denoted by a subscript k, with $k = 0, \ldots, N$. On the other hand, the stresses (and strains) are collocated at each midpoint of the mesh intervals

and denoted accordingly by a subscript $k, k+1$. Two ghost segments, with pedices $-1, 0$ and $N, N+1$, are then added at the ends of the rod, allowing to properly impose the boundary conditions for the stresses. The spatial accuracy of this scheme is investigated in Ref. [31] and it is found to be of second order in the small-displacement regime, consistent with the use of centered finite differences, but to become of first order in the nonlinear regime. This difference is motivated by the presence of quadratic nonlinearities. Given that the position of the rod is a nonlinear function of the system unknowns, it is not obvious to anticipate the corresponding accuracy, but it turns out to coincide with that of the unknowns [31].

As for the time discretisation, we choose to perform the numerical integration by implementing the explicit Runge–Kutta–Dormand–Prince (RKDP) method of order 5(4) with adaptive time-stepping [36]. Such a scheme presents definite advantages over the semi-implicit Euler method used in [31]. It is more accurate, as it provides an approximated solution up to the fourth-order, and it leaves a greater flexibility for the treatment of external forces. The main reason why we need an adaptive time step is the unpredictable nature of the contact interactions in a system where a flexible beam is rotating in a well that is often rather curved. During the dynamics, contact points are constantly changing and the impulse with which the beam reaches the wall can display an erratic intensity. Hence, we need to be able to rapidly reduce the time step when contacts appear. On the other hand, once a rather stationary situation is achieved it is sometimes possible to continue the simulation with a larger time step, saving resources.

It is worth mentioning that the formulation of the equations adopted here expresses everything in terms of unknown fields that take values in the Lie algebra associated with the special Euclidean group. In practice, such a parametrisation keeps the evolution equations within a linear space setting and permits to use less sophisticated integration schemes than those designed to be consistent with evolutions within Lie groups.

In what follows, quantities computed at a discretised time t^n will be denoted by the superscript n. Set $X_k^n = (\Sigma_{k-1,k}^n, P_k^n)$ for $0 < k \leq N$ and $X^n = (X_1^n, \ldots, X_N^n)$, the discretised evolution equations (1)-(2), for inner and free nodes and inner segments, take the form

$$X^{n+1} = X^n + dt^n \sum_{i=1}^{7} b_i \, (K_i)^n,$$

with

$$(K_i)_k^n = f_k \left(t^n + c_i dt^n, \, X^n + dt^n \sum_{j=1}^{i-1} a_{ij} (K_j)^n \right),$$

where the coefficients a_{ij}, b_i and c_i are the entries of the Butcher tableau for the seven-stage RKDP method (reported in Table 1), $dt^n = t^{n+1} - t^n$ is the stepsize for the time integration, and f_k is the function governing the dynamics of the k-th discrete element.

The expressions of the stress and momentum components of $f_k(t^n, X^n) = \left((f^\Sigma)_k^n, (f^P)_k^n\right)$, for $0 < k \leq N$, read, respectively,

$$\begin{aligned}(f^\Sigma)_k^n = {} & \mathbb{A}_k \frac{\mathbb{M}_k^{-1} P_k^n - \mathbb{M}_{k-1}^{-1} P_{k-1}^n}{s_k - s_{k-1}} \\ & + \frac{1}{4} \mathbb{A}_k \, \mathrm{ad}_{U_{k-1,k}^n} (\mathbb{M}_k^{-1} P_k^n + \mathbb{M}_{k-1}^{-1} P_{k-1}^n) \\ & - \frac{1}{4} \mathbb{A}_k \, \mathrm{ad}_{(V_{k-1}^n + V_k^n)} \left(\mathbb{A}_k^{-1} \Sigma_{k-1,k}^n + \bar{U}_{k-1,k} \right)\end{aligned} \tag{4}$$

and

$$\begin{aligned}(f^P)_k^n = {} & \frac{\Sigma_{k,k+1}^n - \Sigma_{k-1,k}^n}{(s_{k+1} - s_{k-1})/2} + \mathrm{ad}_{V_k^n}^\mathsf{T} P_k^n \\ & - \frac{1}{2} \left(\mathrm{ad}_{U_{k-1,k}^n}^\mathsf{T} \Sigma_{k-1,k}^n + \mathrm{ad}_{U_{k,k+1}^n}^\mathsf{T} \Sigma_{k,k+1}^n \right) \\ & - (\mathbb{D}_{\mathrm{ex}})_k^n \mathbb{M}_k^{-1} P_k^n - (\mathbb{D}_{\mathrm{in}})_k^n \mathbb{A}_k^{-1} (f^\Sigma)_k^n + F_k^n\end{aligned} \tag{5}$$

where $U_{k-1,k}^n = \mathbb{A}_k^{-1} \Sigma_{k-1,k}^n + \bar{U}_{k-1,k}$ and $V_k^n = \mathbb{M}_k^{-1} P_k^n$.

The discretised boundary conditions (3) are implemented within the RKDP routine by imposing the following conditions:

$$\begin{aligned} & P_0^{n+1} = \bar{P}_0(t^n + dt^n), \\ & \Sigma_{-1,0}^{n+1} = \Sigma_{0,1}^{n+1}, \\ & \Sigma_{N-1,N}^{n+1} + \Sigma_{N,N+1}^{n+1} = 2\bar{\Sigma}_{\mathrm{e}}(t^n + c_i dt^n), \end{aligned} \tag{6}$$

where, for the segment quantities $\Sigma_{k,k+1}$, the ghost values have been exploited.

The adaptive time step dt^n is iteratively updated so as to keep the error between the fourth- and fifth-order approximations below a chosen threshold. Specifically, the error e^n is estimated as

$$e^n = \sqrt{\frac{1}{12N} \sum_{l=1}^{12N} \frac{\left[\left(\sum_{i=1}^{7} (b_i^* - b_i) \, (K_i)^n \right)_l \right]^2}{\left(10^{-7} + |(X^n)_l| \cdot 10^{-5} \right)^2}},$$

where 10^{-7} and 10^{-5} are picked absolute and relative tolerance factors, respectively, and the subscript l denotes the l-th entry of the corresponding $(12N)$-component vector. If such error is smaller than one, the computed step is accepted and the next stepsize is increased to $dt^{n+1} = dt^n \cdot 0.9 (e^n)^{-1/5}$; if not, the step is repeated with a lower stepsize, taken equal to $dt^n \cdot \min\{\max\{0.9(e^n)^{-1/5}, 10^{-2}\}, 1.5\}$.

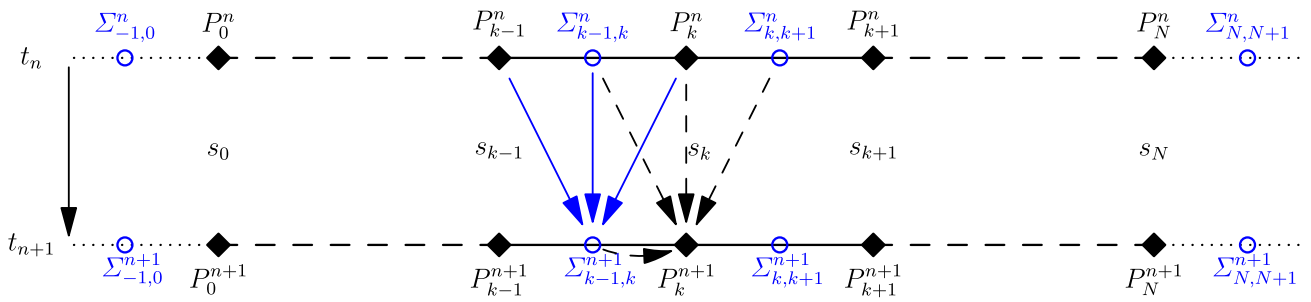

Fig. 2 Discretisation scheme for the evolution equations, based on a finite difference staggered grid for the spatial discretisation and an explicit time integration. The momenta P are assigned to nodes of the partition $0 = s_0 \leq s_1 \leq \cdots \leq s_N = L$ (black diamonds), while the stresses Σ are collocated at the midpoints of the mesh intervals (blue circles). Ghost values $\Sigma^n_{-1,0}$ and $\Sigma^n_{N,N+1}$ are added at the two ends of the domain to impose proper boundary conditions. The momenta P^{n+1}_k at time t^{n+1} at s_k are influenced by the values of the nearest-neighbouring stresses Σ at time t^n and t^{n+1} (black dashed arrows), and the stresses $\Sigma^{n+1}_{k-1,k}$ at $(s_{k-1} + s_k)/2$ are influenced by the nearest-neighbouring momenta P at time t^n (blue solid arrows). (Color figure online)

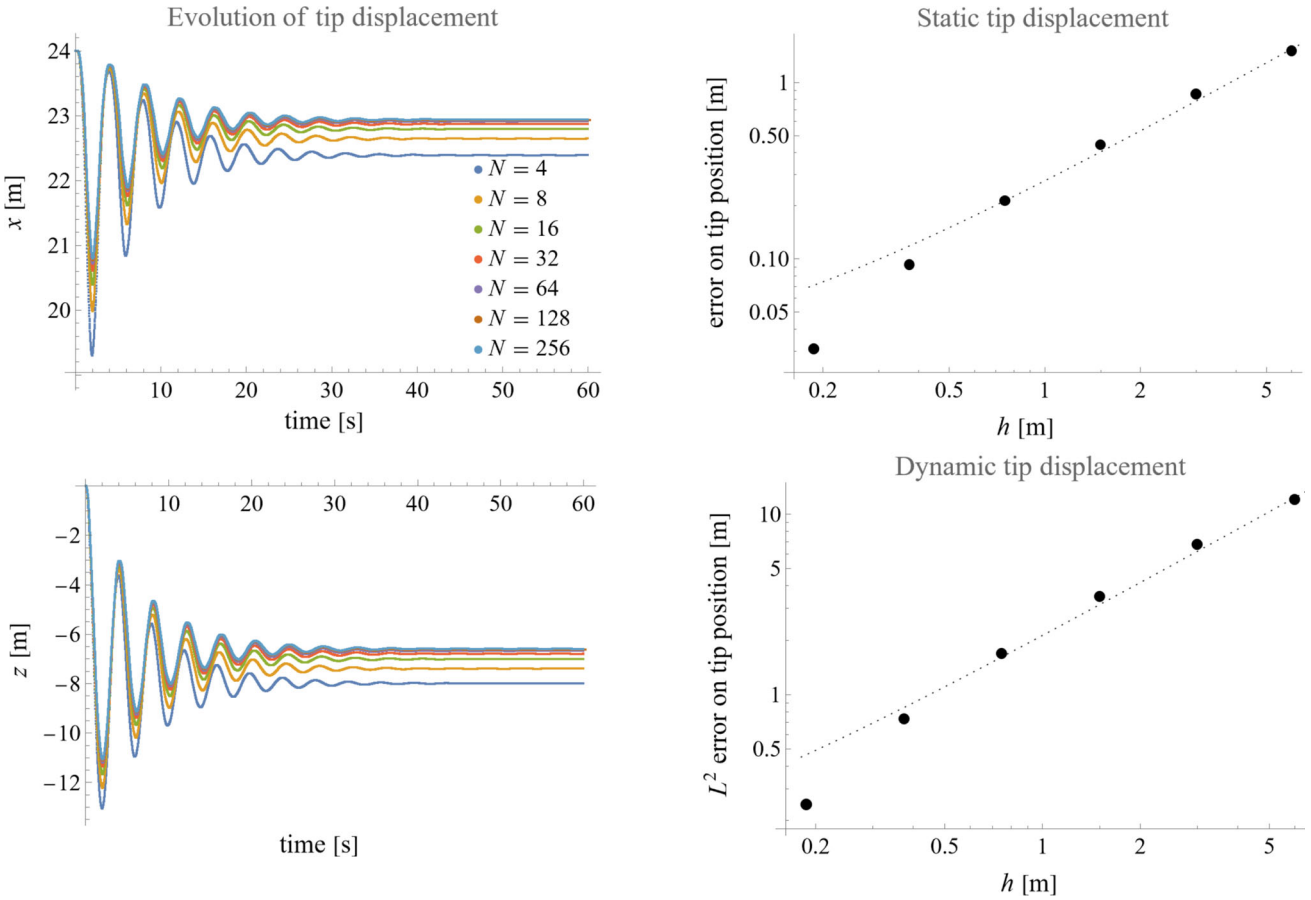

Fig. 3 The numerical solution for the dissipative nonlinear dynamics of a cantilever subject to its own weight (with material parameters given in Table 2), for different refinements of the spatial grid. Left: time evolution of the x and z components of the tip displacement in the vertical plane for different numbers of segments. Right: error estimates on the tip displacement, in the static and dynamic regimes, with respect to the numerical solution obtained for $N = 256$, as a function of the size of the mesh interval $h = L/N$. The dotted lines indicate a linear scaling

Table 1 Butcher tableau for the RKDP method

0							
1/5	1/5						
3/10	3/40	9/40					
4/5	44/55	−56/15	32/9				
8/9	19372/6561	−25360/2187	64448/6561	−212/729			
1	9017/3168	−355/33	46732/5247	49/176	−5103/18656		
1	35/384	0	500/1113	125/192	−2187/6784	11/84	
	35/384	0	500/1113	125/192	−2187/6784	11/84	0
	5179/57600	0	7571/16695	393/640	−92097/339200	187/2100	1/40

The left-most column collects the coefficients c_i, in the lower-triangular matrix in the middle are arranged the coefficients a_{ij}, and the two last rows give, respectively, the coefficients b_i, of the fifth-order accurate solution, and b_i^*, of the fourth-order accurate solution

Table 2 Material parameters for the cantilever test

Parameter	Value
Total relaxed length	24 m
Inner diameter	0.1155 m
Outer diameter	0.1397 m
Linear mass density	34.2277 kg/m
Young modulus	200 GPa
Poisson ratio	0

From equation (5) (resp. (4)), we see that the value of each momentum P_k^{n+1} (resp. stress $\Sigma_{k-1,k}^{n+1}$) at time t^{n+1} is affected by the nearest-neighbouring stresses $\Sigma_{k-1,k}^n$ and $\Sigma_{k,k+1}^n$ (resp. momenta P_{k-1}^n and P_k^n) and by the momenta P_{k-1}^n and P_k^n (resp. stress $\Sigma_{k-1,k}^n$), namely f_k, as a function of X^n, depends on X_{k-1}^n, X_k^n, X_{k+1}^n only. The evolution matrix has hence a band structure, which is exploited in the implementation of the code.

To test the accuracy of the scheme, we considered a hollow cylindrical cantilever, with material parameters given in Table 2, clamped at one end and subject to its own weight. We analysed the scaling of error estimates upon varying the size of the mesh interval. The system was initialised in the straight horizontal configuration and we let it evolve following a dissipative dynamics toward the steady configuration. The dissipation was generated by the internal dissipation matrix $\mathbb{D}_{\text{in}} = \eta_{\text{in}}\text{diag}(1, 1, 1, 1, 1, 1)$, with damping coefficient $\eta_{\text{in}} = 10^{-1}$ N s/m and the external dissipation matrix $\mathbb{D}_{\text{ex}} = \eta_{\text{ex}}\text{diag}(1, 1, 1, 1, 1, 1)$, with damping coefficient $\eta_{\text{ex}} = 10$ Pa s. The spatial discretisation was performed on a uniform grid with a variable number N of intervals, up to $N = 256$ segments.

Figure 3 (left) shows the time evolution of the x and z components of the tip displacement $\boldsymbol{x}(L, t^n)$ in the vertical plane for different values of N. To estimate the order of convergence of our spatial discretisation, we computed, firstly, the absolute error on the stationary tip position, at the final time $t^n = \bar{t}$, for each N with respect to the position reached for the finest mesh used, namely $\left|\boldsymbol{x}^{(256)}(L, \bar{t}) - \boldsymbol{x}^{(N)}(L, \bar{t})\right|$ (top right panel). Secondly, we interpolated the numerical dynamic solution of the tip displacement for each N and computed its L^2-distance, over a continuous time interval, from the displacement obtained with $N = 256$, namely $\left[\int_0^{\bar{t}} \left|\boldsymbol{x}^{(256)}(L, t) - \boldsymbol{x}^{(N)}(L, t)\right|^2 dt\right]^{1/2}$ (bottom right panel). We found, as expected, that both error estimates scale linearly with the size of the mesh interval $h = L/N$ (Fig. 3 (right)).

As for the accuracy in time, the RKDP method provides a fourth-order approximation of the exact dynamics of the system discretised in space. As such, the precision of the time evolution is dominated again by the spatial discretisation, as shown in Figure 3, bottom right panel. In addition, we can observe that the time step necessary to achieve a stable simulation with a more refined grid tends to be smaller than what is needed in the presence of a coarser grid. This is consistent with the need of capturing the wave dynamics across smaller elements. Figure 4 shows the average trend of the adaptive time stepping for each size of the spatial mesh interval h, together with the minimum and maximum step sizes reached in each of the computations.

2.2 The model for the interaction with well and fluids

We now introduce the specifics of drill-string systems and detail our choice for the external dissipative forces and momenta.

The rod will be a slender hollow cylinder, subject to its own weight, which is confined inside a fixed well of a given geometry, with circular cross sections, wider than those of the rod. We refer to the one end of the rod which is connected to the rig at the surface as *head*, and to the opposite end, which is in contact with the bottom of the wellbore, as *bit*. The position and velocity of the head of the rod will be governed by a top drive, while its bit will be free to move inside the well. The annular region between the rod and the well will be filled

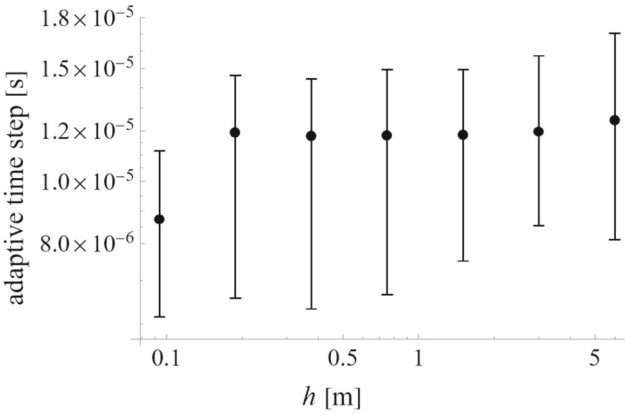

Fig. 4 Dependence of the adaptive time step, generated by the RKDP scheme, on the refinement of the spatial grid. Data points indicate the average step and the bars cover the full range from the minimum to the maximum step size reached in each simulation

with a fluid, with viscosity $\mu > 0$. We model the contact and fluid–structure interactions as time-dependent external forces acting on the system.

We describe the configuration of the well as a time-independent one-parameter family of rigid cross sections labelled by $\hat{s} \in [0, \hat{L}]$, where $\hat{L} > L$ is the length of the well, and we then introduce a partition $\{0 = \hat{s}_0, \ldots, s_{\hat{N}} = \hat{L}\}$ of the spatial domain, with $\hat{s}_k < \hat{s}_{k+1}$. The shape of the well is characterised by the values of the two curvatures given for each segment of the mesh and by the radius $\hat{R}_k$ of each nodal cross section. At variance with the six degrees of freedom that we employ to describe the shape of rod segments, the shape of the well is only encoded in the two curvature components. This is partly due to the geometric nature of the well, for which we do not need to consider a stretching parameter, but mainly to the structure of field data to which we have access. Indeed, it is standard to record the shape of wells as a sequence of circular arcs that interpolate between measured nodal coordinates. As a consequence we can set to zero any twisting or shearing component in the description of the well.

We assume that $\hat{R}_k > R_j$, where R_j denotes the outer radius of the j-th nodal cross section of the rod ($k = 0, \ldots, \hat{N}$, $j = 0, \ldots, N$). To account for the position of the rod relative to the well, we assign, at each node s_k of the discretised rod, a reference basis $(\boldsymbol{r}_k, \boldsymbol{l}_k, \boldsymbol{t}_k)$ which specifies, with respect to the midline curve of the well, the radial direction $\boldsymbol{r}_k$, pointing toward the well midline, the axial direction $\boldsymbol{l}_k$, pointing head-to-bottom, and the azimuthal direction $\boldsymbol{t}_k$, orthogonal to the former ones. We activate the contact interaction of the k-th nodal element of the rod with the constraining well whenever the displacement along $\boldsymbol{r}_k$ of such a node from the midline of the well exceeds the radial clearance between well and rod. We denote by $\Delta r_k \geq 0$ the corresponding penetration and use it as contact detection parameter.

In the following, we present our model for the confined rod, by characterising force and torque densities acting on the rod, which are due to contacts with the well and to the surrounding fluid. The contributions on internal nodes of the mesh are implemented within the code and computed following the dynamics of the rod, as they enter equation (5). On the other hand, the contributions on the head and the bit are included as prescribed boundary conditions, as in equation (6). We start by describing the interaction of the rod with the drilling fluids.

2.2.1 Hydrodynamic interaction with drilling fluids

The fluid, which fills the region delimited by the well, is taken to be viscous, with viscosity μ, and incompressible. The statics of the rod is only affected by the corresponding buoyant force, while the dynamical coupling requires a proper choice of the interaction model. We treat the interaction with the filling fluid which is due to axial translations of the rod as independent of that on cross-sectional planes, due to radial and azimuthal displacements. We refer, for the former, to the classical sliding Couette flow in concentric cylinders, while we adopt, for the latter, the hydrodynamical model proposed by Finn and Cox [32]. On the whole, the method allows us to include an external dissipative contribution due to the fluid interaction in a natural way, which accounts for the position and velocity of the drill-string relative to the borehole. Although in real drilling processes the motion of the fluid is likely turbulent, the slow laminar flow approximation allows us to capture the dissipative hydrodynamical effects on the dynamics of the rod by adjusting the values of effective friction coefficients. In a similar fashion, the presence of additional fluid inside the drilling pipe is taken into account only by calibrating the effective friction coefficients.

To estimate the viscous drag on the rod when it translates longitudinally inside the well, we approximate our model as a system of two infinitely-long circular cylinders in which the inner one slides at a constant speed in the axial direction (see Fig. 5a). We compute the strain exerted by the fluid on the rod, using the well-known result for the stationary flow of an incompressible viscous fluid between the two cylinders [37]. In the absence of external forces and axial pressure gradient, the axial component of the velocity field of the fluid equals $\dot{\boldsymbol{x}}_k^n \cdot \boldsymbol{l}_k^n \log\frac{\hat{R}_k}{r} \left(\log\frac{\hat{R}_k}{R_k}\right)^{-1}$, with r the distance from the axis; hence, we obtain the linear density of axial drag $-D_k^n \boldsymbol{l}_k^n$ with

$$D_k^n := 2\pi\mu \left(\log\frac{\hat{R}_k}{R_k}\right)^{-1} \dot{\boldsymbol{x}}_k^n \cdot \boldsymbol{l}_k^n \,.$$

To account for rotations of the rod and horizontal deviations from the midline of the well, we follow [32], in which the motion of a cylindrical rod inside a larger cylinder

filled with fluid is analysed by describing the system as a translating–rotating mixer (see Fig. 5b). We denote by ε_k^n the eccentricity of the k-th node with respect to the midline of the well at the time t^n and set

$$\sigma_k^n := \left[\frac{\hat{R}^2 - R^2 + \varepsilon^2 + \sqrt{(\hat{R}^2 - R^2 + \varepsilon^2)^2 - 4\varepsilon^2 \hat{R}^2}}{2\varepsilon} \right]_k^n ,$$

$$s_k^n := \frac{\hat{R}^2}{\sigma_k^n} , \qquad \lambda_k^n := \left[\log \frac{\sigma(s-\varepsilon)}{s(\sigma-\varepsilon)} \right]_k^n ,$$

and we define

$$A_k^n := 8\pi\mu \left[\frac{\varepsilon(s+\sigma)(R^2 \varepsilon\, \boldsymbol{\omega}\cdot\boldsymbol{l} - (R^2 + s\sigma)\dot{\boldsymbol{x}}\cdot\boldsymbol{t})}{(\hat{R}^2 - R^2 + \varepsilon^2)(2\varepsilon(\sigma - s) + (\hat{R}^2 + R^2)\lambda)} \right]_k^n ,$$

$$B_k^n := 8\pi\mu \left[\frac{(\varepsilon(s+\sigma) - 2\sigma s)\dot{\boldsymbol{x}}\cdot\boldsymbol{r}}{2\varepsilon(\sigma - s) + (\hat{R}^2 + R^2 - \varepsilon^2)\lambda} \right]_k^n ,$$

$$C_k^n := 4\pi\mu \left[\frac{\hat{R}^2 R^2 (2\varepsilon(\sigma - s) + (\hat{R}^2 + R^2 - \varepsilon^2)\lambda)\boldsymbol{\omega}\cdot\boldsymbol{l}}{\varepsilon(\sigma - s)(2\varepsilon(\sigma - s) + (\hat{R}^2 + R^2)\lambda)} \right]_k^n - 4\pi\mu \left[\frac{2\hat{R}^2 \varepsilon^2 (\sigma - s)\dot{\boldsymbol{x}}\cdot\boldsymbol{t}}{\varepsilon(\sigma - s)(2\varepsilon(\sigma - s) + (\hat{R}^2 + R^2)\lambda)} \right]_k^n .$$

Then, on each cross section of the rod, the fluid exerts a force and a momentum, per unit length, respectively given by

$$\boldsymbol{F}_{\mathbf{hy}}{}_k^n = -\,[\,B\,\boldsymbol{r} + D\,\boldsymbol{l} + A\,\boldsymbol{t}\,]_k^n \tag{7}$$

$$\boldsymbol{M}_{\mathbf{hy}}{}_k^n = -\,[\,(C - \varepsilon A)\,\boldsymbol{l}\,]_k^n \,, \tag{8}$$

namely, with respect to the basis $(\boldsymbol{r}, \boldsymbol{l}, \boldsymbol{t})_k^n$, we get the six-component vector of generalised external forces $-(0, C - \varepsilon A, 0, B, D, A)_k^n$. By defining the change-of-basis matrix $\mathbb{P}_k^n$, through which $\boldsymbol{M}_{\mathbf{hy}}{}_k^n$ and $\boldsymbol{F}_{\mathbf{hy}}{}_k^n$ are projected on the basis $(\boldsymbol{d}_3, \boldsymbol{d}_1, \boldsymbol{d}_2)_k^n$, we obtain the following generalised force density associated with the hydrodynamic contributions:

$$(F_{\mathrm{hy}})_k^n = -\mathbb{P}_k^n \begin{pmatrix} 0 \\ [C - \varepsilon A]_k^n \\ 0 \\ B_k^n \\ D_k^n \\ A_k^n \end{pmatrix} .$$

These contributions are set to zero for those nodes in contact with the well, i.e., whenever $\Delta r_k^n > 0$. In Fig. 5 we give a schematic representation of the sources of hydrodynamic dissipation.

To safeguard the stability of the code, some precaution is required in the implementation of the formulas to manage the almost-touching ($R \to \hat{R}$) and the close-to-concentric

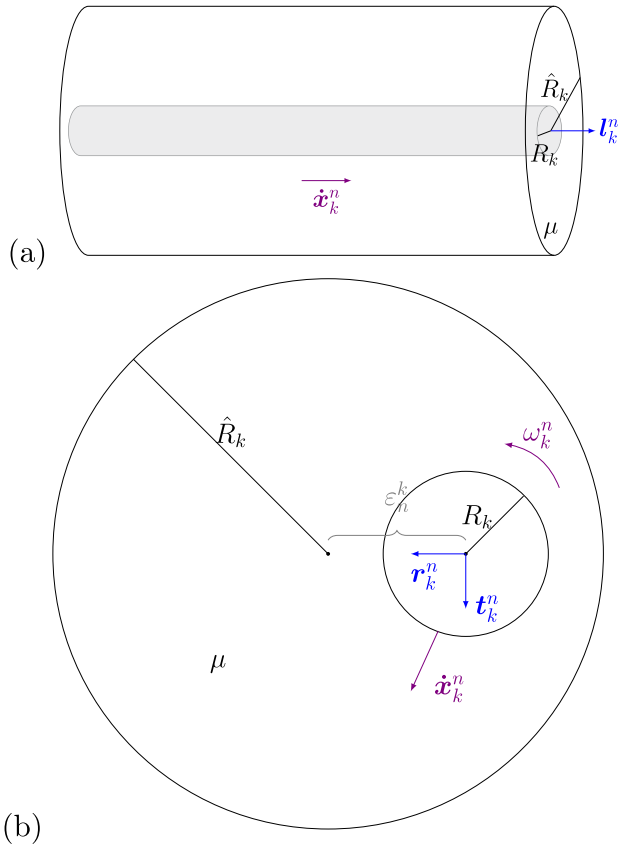

Fig. 5 Schematic representation of the fluid–structure interaction model, based on the slow laminar flow approximation for an incompressible fluid with viscosity μ and on the independence of axial and cross-sectional contributions. The interaction due to the longitudinal motion of the rod inside the well is modelled as sliding flow in two coaxial cylinders (**a**), while the interaction due to radial and azimuthal motion on cross-sectional planes is accounted for via a translating–rotating mixer model (**b**)

($\varepsilon \to 0$) situations, which would produce divergences in equations (7) and (8). We regularise the former by artificially enlarging the radius $\hat{R}_k$; while we deal with the singular limit of vanishing eccentricity by substituting the expressions the coefficients A, B, C, in which $\sigma = \sigma(\varepsilon), s = s(\varepsilon), \lambda = \lambda(\varepsilon)$, with their power series expansion at $\varepsilon = 0$ up to third order, whenever ε falls below a lower threshold, fixed at 10^{-8}.

2.2.2 Contact with the well

To model the dynamic contact interaction between the rod and the well, we adopt a penalty method approach. Namely, we allow for small penetrations between the two objects and model the normal contact forces exerted by the well on the rod as restoring forces produced by elastic springs wherever $\Delta r_k^n > 0$. The energy dissipation during the contact interaction is associated with impact damping and friction at the interfaces opposing the relative motion, and modelled as lin-

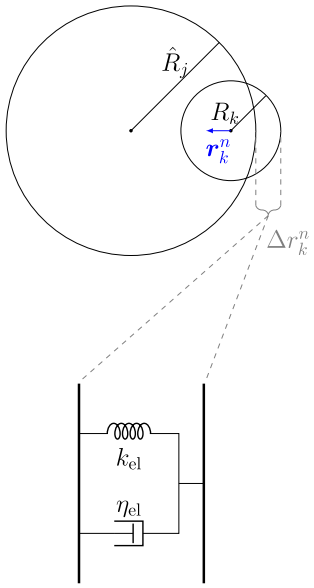

Fig. 6 Schematic representation of the normal contact model based on a penalty method. The circle of radius R_k represents the rod cross section labeled by s_k, while the larger circumference depicts a co-planar section of the well. To model the contact, the method allows a small penetration Δr_k^n along the radial direction $\boldsymbol{r}_k^n$. The normal contact force is given by a spring-dashpot system, which is activated whenever $\Delta r_k^n > 0$

ear viscous dampers and Coulomb friction, respectively. The contact scheme is the following.

In a rather standard way, we describe the unilateral constraint represented by the well, at each node where $\Delta r_k^n > 0$, as a stiff viscoelastic spring, with large elastic constant $(k_{\rm el})_k^n$ and damping coefficient $(\eta_{\rm el})_k^n \geq (k_{\rm el})_k^n$. Namely, on the k-th contacting element will act a normal contact force of spring-dashpot type (see Fig. 6) given by

$$\boldsymbol{F}_{\mathbf{r}k}^n = \left[(k_{\rm el}\ \Delta r - \eta_{\rm el}\ \dot{\boldsymbol{x}} \cdot \boldsymbol{r})\, \boldsymbol{r} \right]_k^n . \tag{9}$$

We then include contact friction forces, which shall model the dynamic dissipative interaction between the rod and well surfaces, as the former slides tangentially (both longitudinally and azimuthally) against the latter. When a new contact is activated, tangential springs in the longitudinal and azimuthal directions are initialised with zero elongation at the contact point. In subsequent movements, if the contact persists, these springs elongate and produce a force on the rod. We account for two distinct contact responses, depending on whether the magnitude of the tangential force in each direction exceeds a static friction threshold proportional to the normal contact force $(k_{\rm el})_k^n \Delta r_k^n$ (see Fig. 7). When the force is below the threshold, the elastic force of the spring only allows for a very small displacement and we are in the *stick* regime. When the force is above the threshold, we enter the *slip* regime by reducing the elongation of the spring in such a way that the new tangential force matches the threshold. In this way we implement a Coulomb friction model. The parameters of this model are the static friction coefficients $\eta_{0,\rm l}$ and $\eta_{0,\rm t}$, which determine the thresholds for the stick response in the longitudinal and azimuthal directions, respectively, and the elastic constant $(k_{\rm tan})_k^n$ of the tangential springs.

More in detail, we define the longitudinal tangent friction force

$$\boldsymbol{F}_{\mathbf{l}k}^n = \left[-k_{\rm tan}\ \Delta\ell_{\rm l}\, \boldsymbol{l} \right]_k^n , \tag{10}$$

where the elongation $(\Delta\ell_{\rm l})_k^n$ of the spring is updated according to the recursion

$$(\Delta\ell_{\rm l})_k^{n+1} = (\Delta\ell_{\rm l})_k^n + dt^n \dot{\boldsymbol{x}}_k^n \cdot \boldsymbol{l}_k^n,$$

and, if $|k_{\rm tan}\Delta\ell_{\rm l}|_k^n > \eta_{0,\rm l}(k_{\rm el}\Delta r)_k^n$, the elongation is updated as

$$(\Delta\ell_{\rm l})_k^{n+1} = \eta_{\rm dy,l} \frac{(k_{\rm el})_k^n}{(k_{\rm tan})_k^n} \Delta r_k^n\ {\rm sgn}\,(\Delta\ell_{\rm l})_k^n,$$

with $\eta_{\rm dy,l}$ the longitudinal dynamic friction coefficient. In this way the force in the slip regime follows a sliding-friction law.

Similarly, we define the azimuthal tangent friction force

$$\boldsymbol{F}_{\mathbf{t}k}^n = \left[-k_{\rm tan}\ \Delta\ell_{\rm t}\, \boldsymbol{t} \right]_k^n , \tag{11}$$

where the elongation of the spring, $(\Delta\ell_{\rm t})_k^n$, is updated according to the recursion

$$(\Delta\ell_{\rm t})_k^{n+1} = (\Delta\ell_{\rm t})_k^n + dt^n R_k\ \boldsymbol{\omega}_k^n \cdot \boldsymbol{l}_k^n,$$

and, if $|k_{\rm tan}\Delta\ell_{\rm t}|_k^n > \eta_{0,\rm t}(k_{\rm el}\Delta r)_k^n$, is computed as

$$(\Delta\ell_{\rm t})_k^{n+1} = \eta_{\rm dy,t}\ R_k\ \frac{(k_{\rm el})_k^n}{(k_{\rm tan})_k^n} \Delta r_k^n\ {\rm sgn}\,(\Delta\ell_{\rm t})_k^n,$$

with $\eta_{\rm dy,t}$ the dynamic friction coefficient along $\boldsymbol{t}$.

The momentum of the force associated with the azimuthal component is then given by

$$\boldsymbol{M}_{\mathbf{t}k}^n = \left[-R\ k_{\rm tan}\ \Delta\ell_{\rm t}\, \boldsymbol{l} \right]_k^n . \tag{12}$$

Therefore, the contribution to external forces and viscous dissipation due to contact with the well is given by

$$(F_{\rm c})_k^n = \mathbb{P}_k^n \begin{pmatrix} 0 \\ -R_k\ (k_{\rm tan}\ \Delta\ell_{\rm t})_k^n \\ 0 \\ (k_{\rm el}\ \Delta r)_k^n \\ -(k_{\rm tan}\ \Delta\ell_{\rm l})_k^n \\ -(k_{\rm tan}\ \Delta\ell_{\rm t})_k^n \end{pmatrix},$$

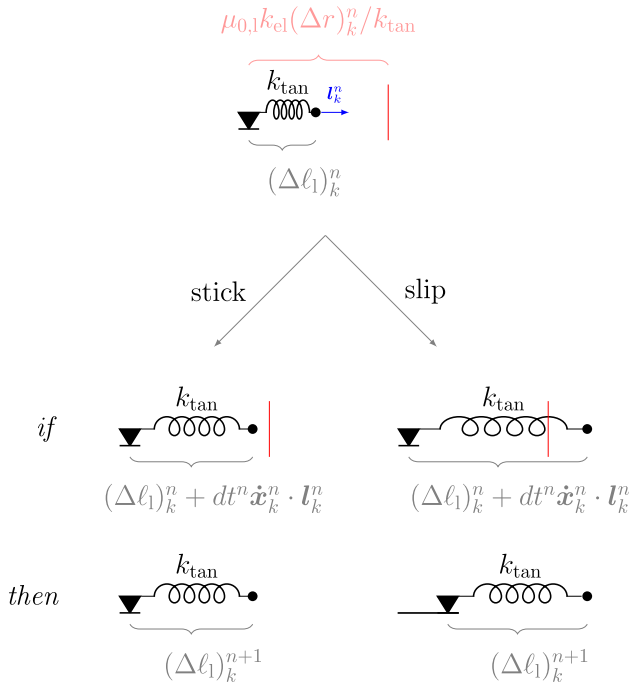

Fig. 7 Schematic representation of the tangential contact model. The elongation of the longitudinal tangential springs, which model the tangential force acting on a rod cross section during a contact with the well, along the longitudinal direction $\boldsymbol{l}_k^n$ can follow two distinct paths. Either stick or slip responses are activated, depending on whether a static friction threshold is exceeded or not. A similar scheme is adopted for the azimuthal direction

$$(\mathbb{D}_{\rm ex,c})_k^n = \mathbb{P}_k^n \begin{pmatrix} 0\,0\,0 & 0 & 0\,0 \\ 0\,0\,0 & 0 & 0\,0 \\ 0\,0\,0 & 0 & 0\,0 \\ 0\,0\,0 & (\eta_{\rm el})_k^n & 0\,0 \\ 0\,0\,0 & 0 & 0\,0 \\ 0\,0\,0 & 0 & 0\,0 \end{pmatrix} (\mathbb{P}^{\mathsf{T}})_k^n .$$

2.2.3 Contacts at the drilling bit

We finally describe the external forces due to the contact of the bit of the drill-string with the bottom of the wellbore. As anticipated, such local interaction is implemented as a given boundary condition for the stresses at the bit, and it depends on the motion prescribed at the head. Our method can be applied for any choice of $\bar{P}_0(t)$, even so, in all the examples which follow, we consider a clamped-free rod with a top-drive which imposes at the head of the rod a component of the angular momentum along the vertical axis with frequency $\omega_{\rm e}(t)$, namely $\bar{P}_0(t^n) = (\omega_{\rm e}(t^n), 0, 0, 0, 0, 0)^{\mathsf{T}}$. To assign a suitable stress at the free end of the rod when subject to a weight on the bit, we assume the bit to be spherically shaped and we model the bit-rock interaction as superposition of an axial force and an axial torque. More specifically, we prescribe the time evolution of the contact force at the free end of the rod, modelled as a compressive load of magnitude $F_{\rm L}(t^n)$, namely

$$\boldsymbol{F}_{\mathbf{wob}}{}_N^{n+1} = [-F_{\rm L}(t)\, \boldsymbol{d_3}]_N^{n+1} , \tag{13}$$

and we assume that a dissipative force arises from Coulomb friction. When a rotational speed is imposed, such friction activates a torque, proportional to the load, which opposes the external rotational drive. In order to compute the momentum of the Coulomb force produced by the external load, we assume the latter to be homogeneously distributed on the bit surface, so that

$$\boldsymbol{M}_{\mathbf{wob}}{}_N^{n+1} = \big[-\operatorname{sgn}(\omega_{\rm e}(t)) M_{\rm L}(t)\, \boldsymbol{d_3}\big]_N^{n+1} , \tag{14}$$

where the magnitude $M_{\rm L}$ is given by

$$\begin{aligned} M_{\rm L}(t) &= \int_{-R}^{0} \int_{0}^{2\pi} \sqrt{R^2 - z^2}\, \mu_{\rm b} \frac{F_{\rm L}(t)}{2\pi R}\, d\varphi\, dz \\ &= \mu_{\rm b} \frac{\pi R}{4} F_{\rm L}(t), \end{aligned} \tag{15}$$

with $\mu_{\rm b}$ a friction coefficient. The stress prescribed at the bit reads

$$\Sigma_{\rm e}(t^{n+1}) = \begin{pmatrix} -\operatorname{sgn}(\omega_{\rm e}(t^{n+1})) M_{\rm L}(t^{n+1}) \\ 0 \\ 0 \\ -F_{\rm L}(t^{n+1}) \\ 0 \\ 0 \end{pmatrix} .$$

3 Application to buckling analysis

The identification of safe operating conditions for the drill-string system requires accuracy in capturing the response of the drill-string when a compressive load is applied at the bit, as it might affect the structural integrity of the pipe. To this end, we provide an analytical validation of the discretisation scheme of the model of rod adopted, through a linear stability analysis of the straight equilibrium configuration and eigenmode analysis. Thereafter, constrained post-buckling configurations are analysed, relying on numerical simulations for representative values of drilling systems. The material parameters for the systems considered are given in Table 3.

3.1 Modal analysis for unconstrained buckling

We verify that the spatially-discretised rod model [31] accounts correctly for Euler's buckling when a compressive load is applied at one end of the rod, having clamped the

Table 3 Material parameters of the rod and the well for the numerical simulations presented in Sect. 3

Rod	
Parameter	**Value**
Total relaxed length	1 km
Inner diameter	0.12 m
Outer diameter	0.14 m
Linear mass density	31.8557 kg/m
Young modulus	200 GPa
Poisson ratio	0
Well	
Parameter	**Value**
Length	1.1 km
Diameter	0.22 m
Fluid density	1000 kg/m^3

other one. To this end, we derive the equilibrium configuration for a vertical rod subject to its own weight and a constant compressive force at the free end, and we study the stability of such equilibrium by means of a linear analysis.

We fix the following notation, slightly adapted from [31], denoting by a superscript (k) quantities referring to the k-th interval of the spatial discretisation introduced in Sect. 2.1.2, namely both nodal (with subscript k) and segment (with subscript $k-1, k$) quantities. The length of the k-segment is indicated by $ds^{(k)}$ and the associated strain vector by $U^{(k)} = (U_1^{(k)}, \dots, U_6^{(k)})$, where the components are, respectively, the twist density, the curvatures, the stretching, and the shearing densities. In a (4×3)-matrix representation, the placement of the k-th element of rod is identified by $\mathcal{P}^{(k)} = (\boldsymbol{x}^{(k)}, \boldsymbol{d}_3^{(k)}, \boldsymbol{d}_1^{(k)}, \boldsymbol{d}_2^{(k)})^\mathsf{T}$ and the strains are collected in the matrix $\mathsf{L}^{(k)}$, which is assumed to be constant on the k-th segment. The placement of the whole rod can be iteratively reconstructed from $\mathcal{P}^{(0)}$, via the exponential map: $\mathcal{P}^{(k)} = \exp(ds^{(k)}\mathsf{L}^{(k)})\mathcal{P}^{(k-1)}$, with

$$\begin{aligned}\exp(ds^{(k)}\mathsf{L}^{(k)}) = \mathsf{Id} &+ ds^{(k)}\mathsf{L}^{(k)} + \frac{1-\cos\theta^{(k)}}{(\theta^{(k)})^2}(ds^{(k)}\mathsf{L}^{(k)})^2 \\ &+ \frac{\theta^{(k)} - \sin\theta^{(k)}}{(\theta^{(k)})^3}(ds^{(k)}\mathsf{L}^{(k)})^3,\end{aligned}$$

and

$$\theta^{(k)} := ds^{(k)}\sqrt{(U_1^{(k)})^2 + (U_2^{(k)})^2 + (U_3^{(k)})^2}.$$

We consider boundary conditions in which one end of the rod, $\mathcal{P}^{(0)}$, is clamped, while the opposite one, $\mathcal{P}^{(N)}$, is free to move. At this latter end, a compressive load of magnitude F_L is applied. Each element is also subject to its own weight and, without much loss of generality, we take the inertia and stiffness matrices constant and uniform.

Being the introduced external forces conservative, an equilibrium configuration and its stability properties can be derived by the first and second variations in $U^{(k)}$, for $k = 1, \dots, N$, of the potential energy

$$\begin{aligned}\mathcal{U} = &\sum_{p=1}^{N}\left[\frac{1}{2}(U^{(p)} - \bar{U}^{(p)}) \cdot \mathbb{A}(U^{(p)} - \bar{U}^{(p)})ds^{(p)}\right] \\ &- \sum_{p=1}^{N}\left[\rho\, g\, ds^{(p)}\, \mathcal{P}_{13}^{(p)}\right] + F_\mathrm{L}\, \mathcal{P}_{13}^{(N)},\end{aligned}$$

where ρ is the linear mass density, g the gravitational constant, and the subscript "13" denotes the component x_3 of the placement of p-th cross section of the rod. For the reference strain $\bar{U}^{(k)} = (0, 0, 0, 1, 0, 0)$, $k = 1, \dots, N$, we get the following equilibrium $U^{(k)\star} = (U_1^{(k)\star}, \dots, U_6^{(k)\star})$ with $U_{i\neq 4}^{(k)\star} = 0$ and

$$U_4^{(k)\star} = 1 - (EA)^{-1}\left[F_\mathrm{L} - \sum_{p=k}^{N}\rho\, g\, ds^{(p)}\right], \tag{16}$$

where $EA = (\mathbb{A})_{44}$, with E the Young modulus and A the area of the rod cross section. This equilibrium shape corresponds to a straight rod.

At the equilibrium (16), we get the matrix of the linearisation, $\Lambda \in \mathrm{Mat}_{6N\times 6N}(\mathbb{R})$, which has a block structure, where the diagonal blocks $\Lambda^{(k)}$ and out-of-diagonal blocks $\Lambda^{(lk)}$, for $k, l = 1, \dots, N$, have the following (ij)-th entry, respectively:

$$\begin{aligned}\Lambda_{ij}^{(k)} = &\mathbb{A}_{ij}ds^{(k)} + \frac{(ds^{(k)})^2}{2} \\ &\cdot\left[F_\mathrm{L}(\mathsf{Id} + \sigma^{(kN)}\hat{\mathsf{L}}_4) - \sum_{p=k}^{n}\rho\, g ds^{(p)}(\mathsf{Id} + \sigma^{(kp)}\hat{\mathsf{L}}_4)\right] \\ &\cdot(\hat{\mathsf{L}}_i\hat{\mathsf{L}}_j + \hat{\mathsf{L}}_j\hat{\mathsf{L}}_i)\,\mathcal{P}_{13}^{(0)}\end{aligned}$$

for $l > k$:

$$\begin{aligned}\Lambda_{ij}^{(lk)} = &ds^{(l)}ds^{(k)} \\ &\cdot\left[F_\mathrm{L}(\mathsf{Id} + \sigma^{(lkN)}\hat{\mathsf{L}}_4) - \sum_{q=l}^{n}\rho\, g ds^{(q)}(\mathsf{Id} + \sigma^{(lkq)}\hat{\mathsf{L}}_4)\right] \\ &\cdot\hat{\mathsf{L}}_i\hat{\mathsf{L}}_j\,\mathcal{P}_{13}^{(0)}\end{aligned}$$

for $l < k$:

$$\Lambda_{ij}^{(lk)} = ds^{(l)} ds^{(k)} \cdot \left[F_{\mathrm{L}} (\mathsf{Id} + \sigma^{(klN)} \hat{\mathsf{L}}_4) - \sum_{q=k}^{n} (\rho\, g ds^{(q)}\, \mathsf{Id} + \sigma^{(klq)} \hat{\mathsf{L}}_4) \right] \cdot \hat{\mathsf{L}}_j \hat{\mathsf{L}}_i\, \mathcal{P}_{13}^{(0)}$$

where $\sigma^{(kp)} := \sum_{q=k+1}^{p} ds^{(q)} U_4^{(q)\star} + \frac{ds^{(k)}}{3} U_4^{(k)\star}$ and $\sigma^{(lkq)} := \sum_{r=l+1}^{q} ds^{(r)} U_4^{(r)\star} + \frac{ds^{(l)}}{2} U_4^{(l)\star}$, and $\hat{\mathsf{L}}_h$, for $h = 1, \ldots, 6$, are 6×6 constant matrices such that $\mathsf{L}^{(k)} = \sum_{h=1}^{6} U_h^{(k)} \hat{\mathsf{L}}_h$.

In the absence of load, with $F_{\mathrm{L}} = 0$, the matrix Λ is positive definite and the equilibrium $U^\star$ is stable. As $F_{\mathrm{L}} > 0$ reaches a critical threshold F_{cr}, a pair of eigenvalues of Λ becomes negative and the equilibrium has a two-dimensional unstable eigenspace, which corresponds to the first buckling mode. As F_{L} increases, an increasing number of eigenvalues become negative, and, correspondingly, further buckling modes appear. As to be expected, each eigenvalue has a degeneracy equal to two, which is due to the rotational invariance of the system about the vertical axis.

In the following, a numerical validation of the model is provided by determining buckling thresholds, for values of the material parameters given in Table 3. Further details of buckling phenomena are discussed, relying on this linear analysis.

3.1.1 Comparison with Euler's critical load for negligible weight

For a weightless, one-end-clamped rod of relaxed length L, the Euler–Bernoulli beam theory predicts the following critical load

$$P_{\mathrm{cr}} = \frac{\pi^2 E I_1}{(2\,L)^2},$$

where I_1 is the second area moment. For the set of material parameters we chose (see Table 3), the expected value is $P_{\mathrm{cr}} = 4.2827$ N. We verified the convergence of the critical load F_{cr}, which depends on the refinement of the spatial grid, to P_{cr}. Figure 8 indicates that the threshold obtained by the discretised model converges fast to the expected value, as the relative error $(F_{\mathrm{cr}} - P_{\mathrm{cr}})/P_{\mathrm{cr}}$ is below 1% already for $N = 5$.

Further buckling modes and eigenstates. The values of the critical load that we obtained for further buckling modes are still in good agreement with Euler's prediction, as they grow quadratically with the mode number $n \in \mathbb{N}$, for odd values of n (for n even, due to the degeneracy of the eigenvalues of Λ, the critical load is the one corresponding to $n - 1$).

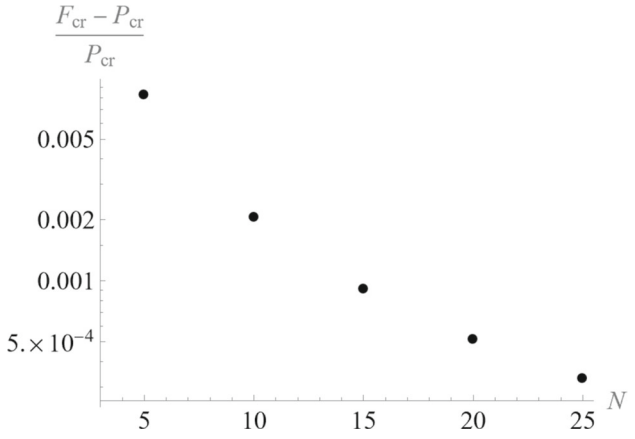

Fig. 8 Relative error between the critical load F_{cr} predicted by our model and Euler's critical value P_{cr}, for a weightless rod clamped at one end (with material parameters given in Table 3), as a function of the number N of segments. For any N, F_{cr} is the minimal value of the compressive load applied at the free end of the rod which makes the equilibrium (16) unstable, in the absence of gravity. The semi-log plot indicates a fast convergence of the critical value F_{cr} predicted by our model to the expected value P_{cr} as the refinement of the spatial grid increases. In fact, the relative error is below 1% already for $N = 5$

Fixed $N = 20$, the computed values of the critical load are 38.7233 N, for the mode $n = 3$, and 103.450 N for $n = 5$. The relative error between the expected threshold and the one computed, however, increases with n: it equals 0.5% for $n = 3$ and 3% for $n = 5$. This is to be expected since higher buckling modes are more sensitive to the discretisation refinement.

Figure 9 shows the profiles, for various buckling modes, of the component of the strains eigenvector associated with the bending $U_2^{(k)}$, at each discrete element $k = 1, \ldots, N$, for $N = 20$. The buckling interests the whole rod's length and, in particular, in the first mode, the bending is greater close to the clamped end. Moreover, the profiles associated with the bending $U_3^{(k)}$ are the same as those of $U_2^{(k)}$ (they differ at most for a rescaling). Hence, the unconstrained buckling that we observe is planar.

Contribution of the shear. The expected Euler's critical load to which we referred derives from a model of rod in which the strains associated with the shearing are assumed to be zero; on the other hand, the model we adopted accounts intrinsically for them. Even so, as discussed above, we found critical thresholds comparable to Euler's loads, which indicates that, for the material parameters we fixed, the shearing components of the strain are negligible with respect to the bending ones. Indeed, we are considering a slender structure.

For comparison, Fig. 10 depicts the components of the eigenstates corresponding to the first buckling mode associated with the bending U_2 (circles) and the shearing U_5 (squares), for the set of parameters given in Table 3

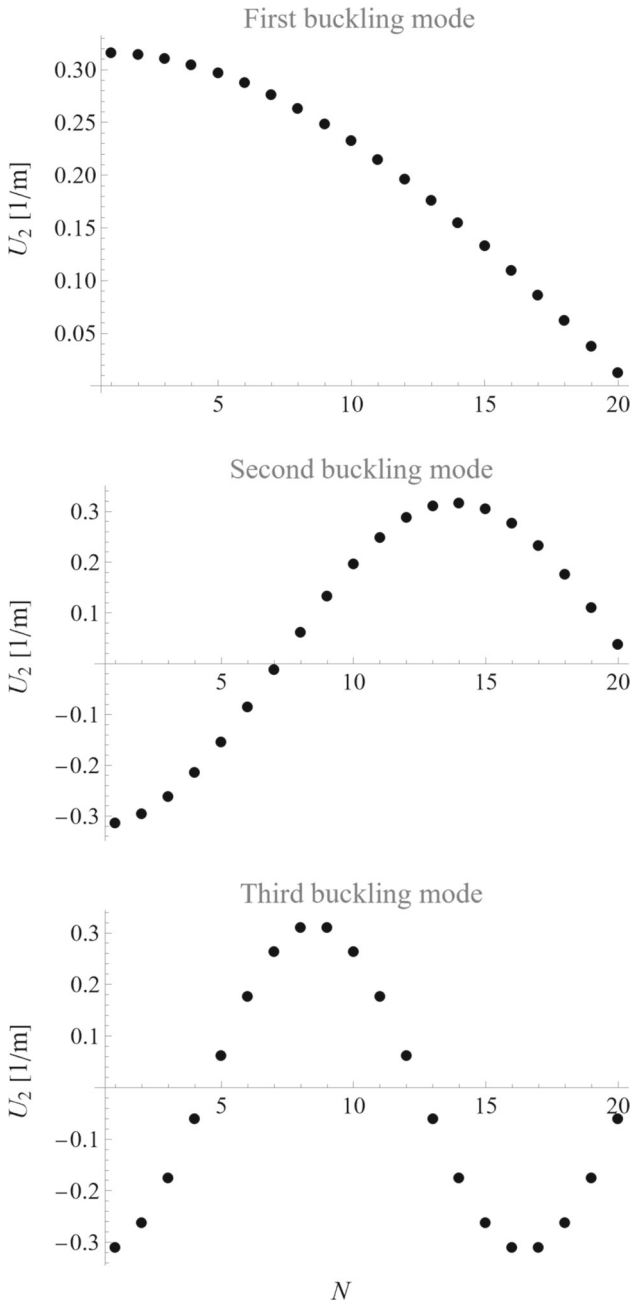

Fig. 9 Profiles of the component of the strains associated with the bending $U_2^{(k)}$, $k = 1, \ldots, 20$, for the system linearised about the equilibrium configuration $U^{(k)\star}$, in the absence of gravity and in the presence of an external force equal to the corresponding critical load

(top panel) and for a rod of length 1 m (bottom panel). The shearing, which in the former case is negligible with respect to the bending, becomes more relevant for a rod with a low slenderness ratio.

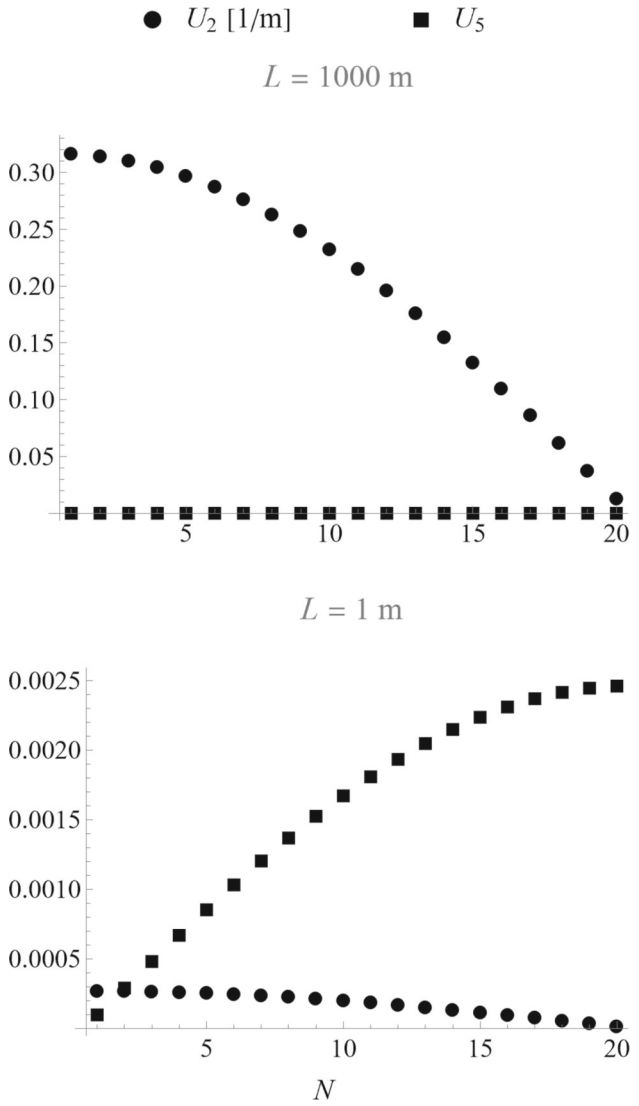

Fig. 10 Profiles of the components of the strains eigenvectors, for the linearised system, associated with the bending $U_2^{(k)}$ and the shearing $U_5^{(k)}$, $k = 1, \ldots, 20$, in the absence of gravity and in the presence of an external force equal to the critical load. The plot at the top refers to the set of material parameters given in Table 3, while at the bottom are shown the profiles for a rod whose length is a thousand time shorter

3.1.2 Contribution of the weight

The inclusion of gravity entails two major modifications on the buckling modes: first, the critical threshold becomes significantly higher, and second, the bending interests only a few elements of the rod, which are the closest to the free end, as it takes large values of the load to affect those parts closer to the clamped end.

Figure 11 indicates that a finer grid for the discretised rod is now required, as it takes about $N = 60$ elements to get a relative error below 10%. The same figure, which displays the semi-log graph with log-linear scale, suggests that the

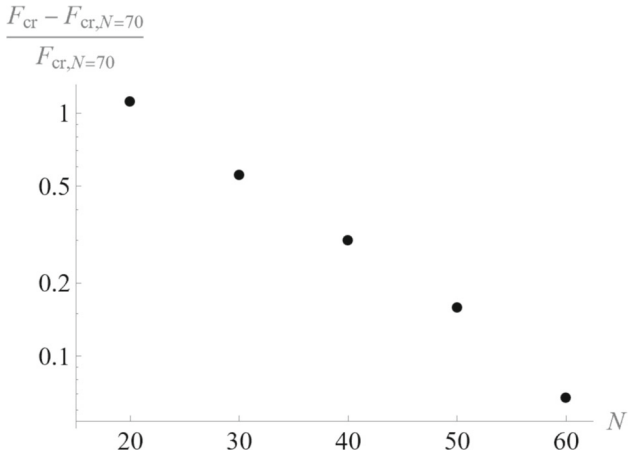

Fig. 11 Relative error between the critical load F_{cr} and the chosen reference value $F_{cr,N=70}$, computed with $N = 70$ elements, for a heavy rod clamped at one end (with material parameters given in Table 3), as a function of the number N of segments. For any N, F_{cr} is the minimal value of the compressive load applied at the free end of the rod which makes the equilibrium (16) unstable, in the presence of gravity. The semi-log plot indicates an exponential scaling of the relative error as the refinement of the spatial grid increases. For $N = 70$, the predicted magnitude of the critical load in the presence of gravity is $F_{cr,N=70} = 8243.18$ N, which is significantly larger than the corresponding value $P_{cr} = 4.2827$ N expected for the weightless rod

scaling of such error is exponential. The critical value of the load for the first buckling mode computed at $N = 70$ is $F_{cr,N=70} = 8243.18$ N, which is about $2 \cdot 10^3$ times as large as Euler's threshold for the corresponding weightless rod.

In the absence of external loads, the heavy vertical rod would relax to a stretched configuration, in which the placement of the k-th element is $\mathcal{P}_g^{(k)} = \sum_{l=1}^{k} ds^{(l)} \left(1 + (EA)^{-1} \sum_{p=l}^{N} \rho g ds^{(p)}\right)$, and the overall length equals $\mathcal{P}_g^{(N)}$. For the considered material parameters, such contribution corresponds to an elongation of about 0.2 m. When the load is applied, since the weight introduces a strain associated with the stretching which is greater the closer to the head, the response of the rod is non-uniform. In particular, the elements of the rod closer to the bit will be the first to be compressed and, possibly, to buckle. Specifically, expression (16) implies that for the N-th element to be compressed it is required a load greater than $\rho g ds^{(N)}$. Dually, provided a uniform discretisation, the number of discrete elements that are compressed, for a given load F_L, is the integer part of $F_L/(\rho g ds^{(N)})$. The critical value of the load is now the sum of the force required to counteract gravity and the value of Euler's critical load which corresponds to a rod of length equal to the portion of the rod which is compressed. The components of the strains eigenvector associated with the bending $U_2^{(k)}$, for $k = 1, \ldots, N = 50$, are shown in Fig. 12.

3.2 Simulations of constrained buckling

We then analysed the static solutions for a rod, with uniform mass density, clamped at the head, inserted inside cylindrical wells, and subjected to compressive loads of different magnitudes at its bit. The material parameters for the systems considered are given in Table 3. The spatial discretisation was performed on a uniform grid with $N = 200$ segments. Internal dissipation was included by assigning the matrix $\mathbb{D}_{in} = \eta_{in}\text{diag}(1, 1, 1, 1, 1, 1)$, with damping coefficient $\eta_{in} = 10^{-2}$ N s/m. The constraint was attained via viscoelastic springs with coefficients $k_{el} = 10^5$ Pa and $\eta_{el} = 10^6$ Pa s, while the value $k_{tan} = 10$ Pa was chosen for the tangential springs, together with the friction coefficients $\eta_{0,l} = \eta_{0,t} = 0.6$ and $\eta_{dy,l} = \eta_{dy,t} = 0.42$. The (very large) value $\mu = 1$ Pa s for the fluid viscosity was fixed to reach quickly the static regime.

We considered wells with either vertical or horizontal axes. For both settings, we initialised the system with conditions close to the equilibrium configuration, let the system evolve for 5 s and verified that the rod was sufficiently relaxed; we then applied at the bit a compressive load with linearly increasing magnitude for 5 s up to a value $\bar{F}$, and, finally, fixed $\bar{F}$, we let the motion evolve up to a time $\bar{t}$ sufficiently long to observe the steady solution. Sufficiently large values for $\bar{F}$ were chosen, so as to observe constrained buckling. In all cases, the adaptive time step settles around 10^{-5} s and the convergence to a static solution was obtained within $5 \cdot 10^5$ steps. Through this analysis, we find confirmation that the method adopted is able to capture deformations which are highly non-linear and we infer relevant characteristics of post-buckling states.

3.2.1 Vertical well

Figure 13 depicts a three-dimensional representation of the midline displacement of the rod in post-buckling configurations, reached following a dissipative dynamics for the rod confined inside a vertical well. For this setting, the well and the rod were coaxial, in a vertical configuration, and the motion of the rod was initialised with small uniform curvature (10^{-7} m^{-1}) and twisting (10^{-6} m^{-1}). The magnitudes of the load chosen for the simulations were (a) $\bar{F} = 20$ kN, (b) $\bar{F} = 50$ kN, (c) $\bar{F} = 100$ kN.

The numerical simulations indicate that the critical values of the load, above which the rod buckles in such a constrained configuration, are of the same order of magnitude as those for the unconstrained system, which is about 10 kN. Similarly to the unconstrained setting, the buckling interests the portion of rod which is compressed, but now the confinement of the well favours buckled configurations which are non-planar. In Fig. 14, the components of the stresses associated with bending are compared for the three values of the load considered.

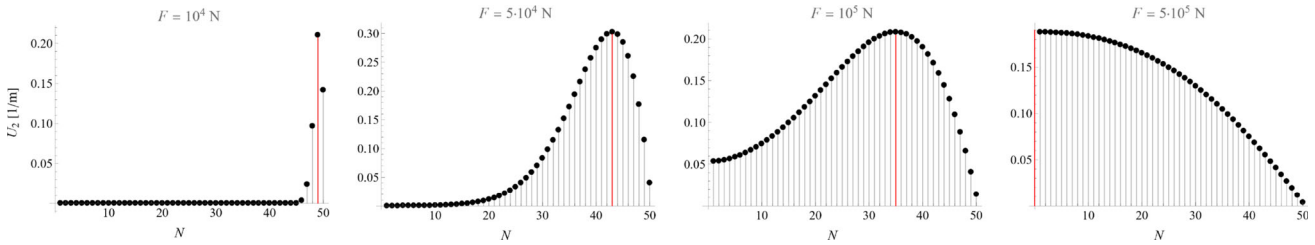

Fig. 12 Profiles of the components of the strains eigenvectors, for the linearised system, associated with the bending $U_2^{(k)}$, $k = 1, \ldots, N = 50$, in the presence of gravity and external force equal to (from left to right) 10 kN, 50 kN, 100 kN, and 500 kN. Highlighted in red, the value above which the rod is compressed. (Colour figure online)

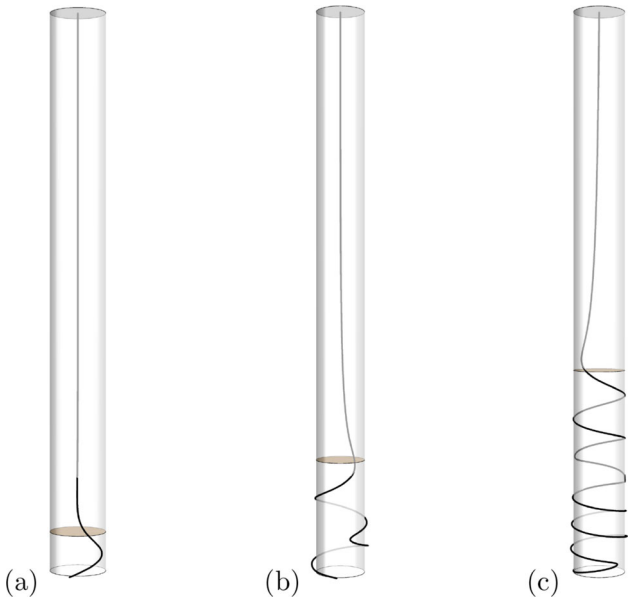

Fig. 13 Three-dimensional representation of the midline (black curve) of the rod inserted in the vertical well (the shadowed cylinder depicts the radial clearance between the rod and the well), in the presence of gravity and subject to a compressive load of magnitude, respectively, **a** $\bar{F} = 20$ kN, **b** $\bar{F} = 50$ kN, **c** $\bar{F} = 100$ kN. The highlighted section of the cylinder marks the portion below which the rod is compressed

In particular, the helical structure is detectable by the two bendings being out-of-phase.

The method allows to obtain further information on the type of buckling by analysing the angle spanned by the radial component of the contact forces along the whole length of the rod. These profiles are presented in Fig. 15, in which a helical-shaped post-buckling configuration is detectable whenever an angle multiple of 2π is spanned, and the number of spirals equals the quotient of the 2π-modulo. The results indicate that helical buckling settles as soon as the rod first collides with a side of the well and that the helical structure, whose winding direction depends on the initial twisting, might present one or more helix reversals.

3.2.2 Horizontal well

Figure 16 depicts a three-dimensional representation of the midline displacement of the rod in post-buckling configurations, reached following a dissipative dynamics for the rod confined inside a horizontal well. In this setting, the system was initialised with the rod at its relaxed state leaning against the bottom of the well, with a small lateral offset (10^{-2} m) of the two axes. The magnitudes of the load chosen for the simulations were (a) $\bar{F} = 350$ kN, (b) $\bar{F} = 500$ kN, (c) $\bar{F} = 1$ MN.

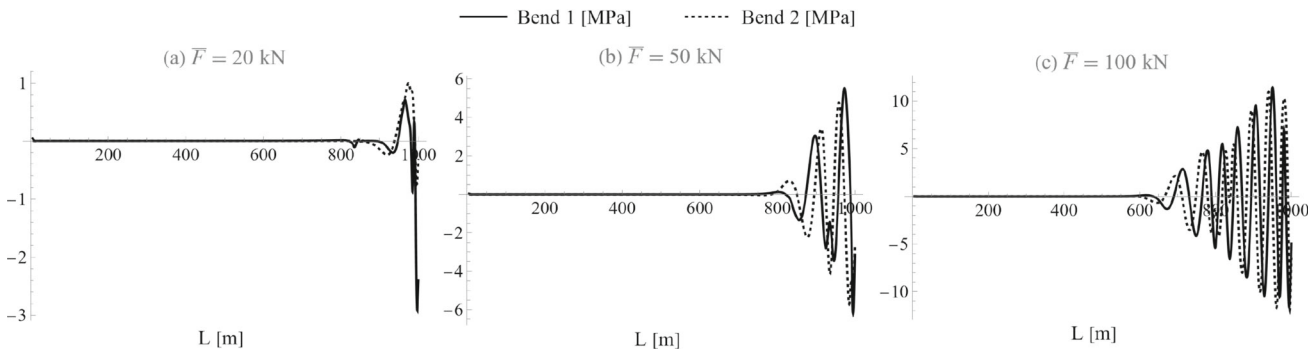

Fig. 14 Profiles of the components of the stresses associated with bending, for the rod inserted in the vertical well, in the presence of gravity and subject to a compressive load of magnitude, respectively, **a** $\bar{F} = 20$ kN, **b** $\bar{F} = 50$ kN, **c** $\bar{F} = 100$ kN

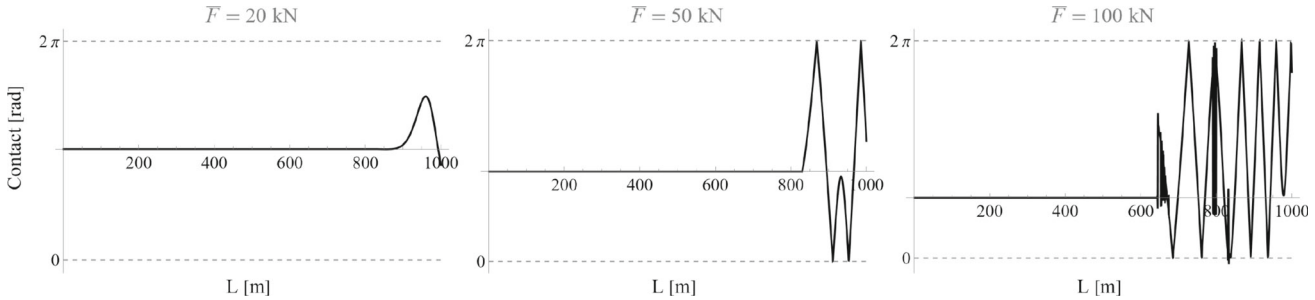

Fig. 15 Profile of the angular component of the contact forces exerted by the vertical well on the rod. At the bit of the rod is applied a compressive load, with increasing magnitude (left to right), and each panel depicts a post-buckling configuration, which is sinusoidal when the plotted function does not reach one of the two horizontal dashed lines, otherwise helices are present

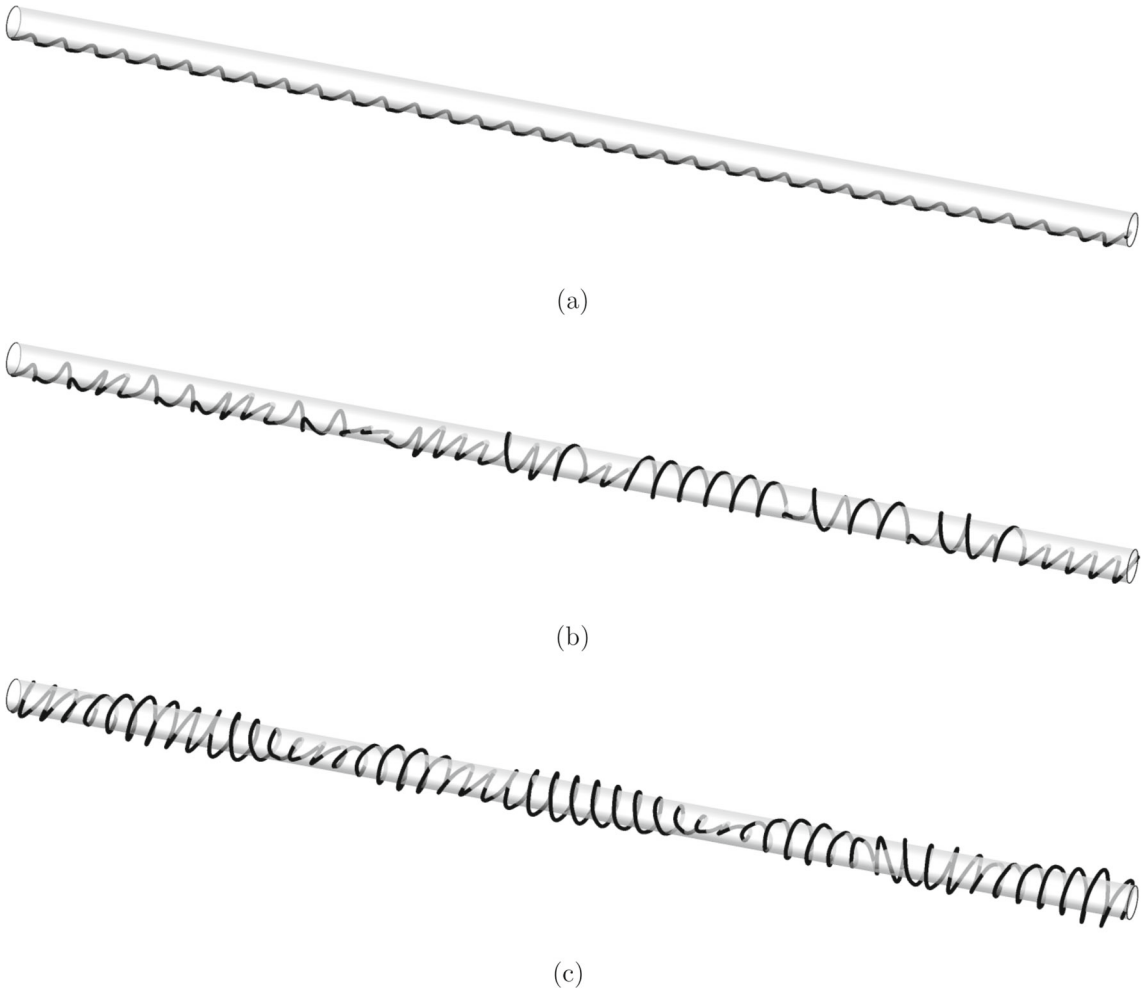

Fig. 16 Three-dimensional representation of the midline (black curve) of the rod inserted in the horizontal well (the shadowed cylinder depicts the radial clearance between the rod and the well), in the presence of gravity and subject to a compressive load of magnitude, respectively, **a** $\bar{F} = 350$ kN, **b** $\bar{F} = 500$ kN, **c** $\bar{F} = 1$ MN

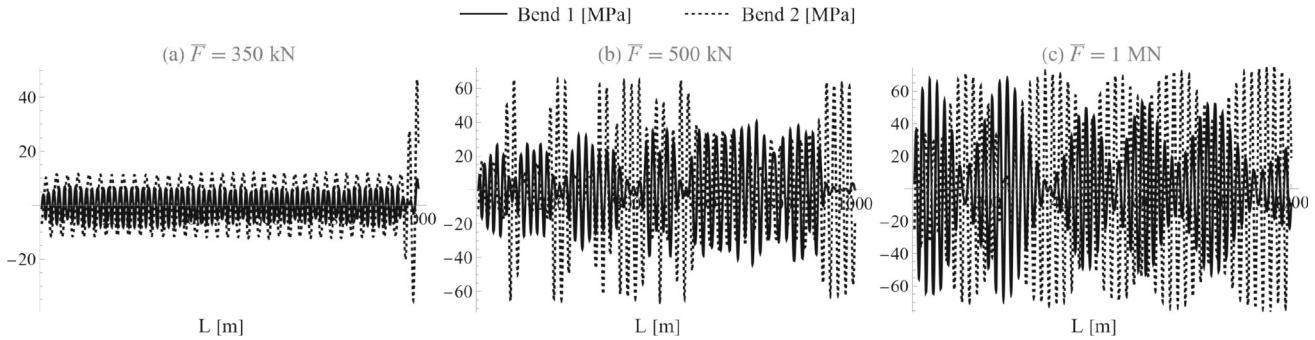

Fig. 17 Profiles of the components of the stresses associated with bending, of the rod inserted in the horizontal well, in the presence of gravity and subject to a compressive load of magnitude, respectively, **a** $\bar{F} = 350$ kN, **b** $\bar{F} = 500$ kN, **c** $\bar{F} = 1$ MN

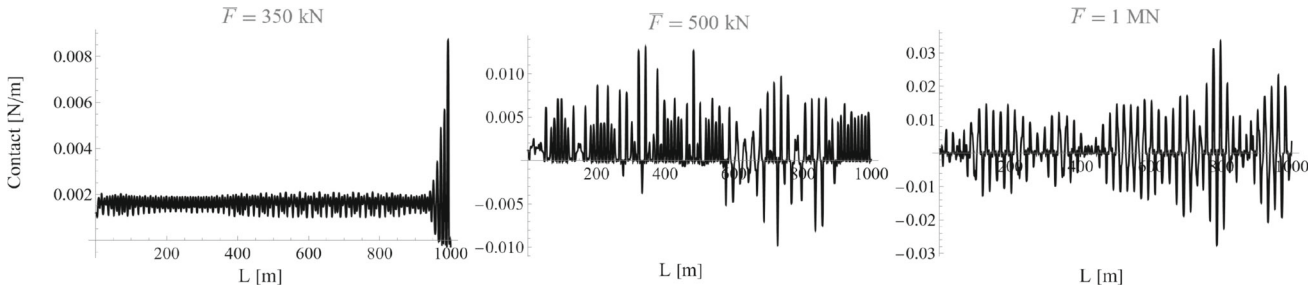

Fig. 18 Profile of the component along the vertical axis of the contact forces exerted by the well on the rod. At the bit of the rod is applied a compressive load, with increasing magnitude (left to right), and each panel depicts a post-buckling configuration, which is sinusoidal when the plotted function always remains positive, while it is (partially) helical wherever negative values are attained

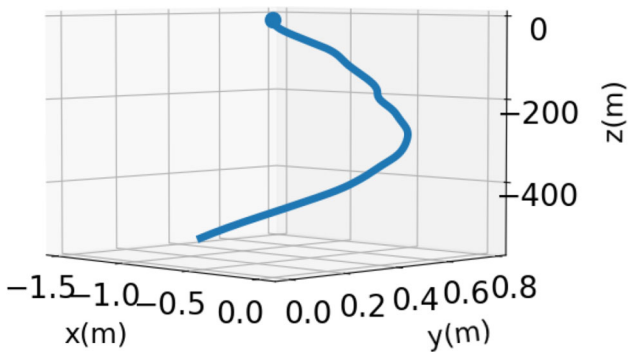

Fig. 19 Three-dimensional representation of the profile of well identified as *Well 1*. Note that the scale on the vertical component is much larger than the others, namely the well is practically vertical

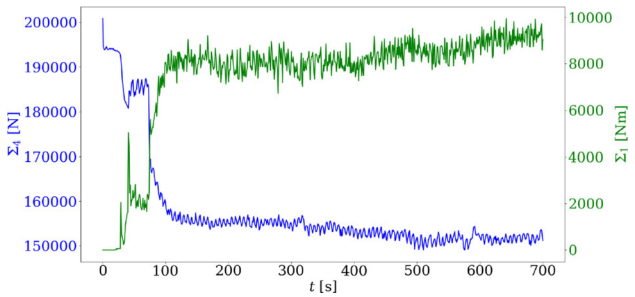

Fig. 20 Measurements collected in drilling operations in the well named *Well 1*. The blue and green signals represent the time evolution of the stresses Σ_4 and Σ_1 associated with stretching and twisting, respectively, registered at the head of the drill-string. (Color figure online)

For the horizontal configuration, the weight hinders buckled states, which appear to be stable for values of loads about one order of magnitude greater than the one detected for the vertical configuration discussed in the previous section. Figure 16 shows some of the post-buckling configurations attained for different loads, while in Fig. 17 the components of the stresses associated with bending are compared. For the horizontal configuration, both sinusoidal and helical buckling are observed, as well as combinations of the two. Further information about the type of buckling was obtained by analysing the component of the contact forces along the vertical. Mostly, the vertical component of the contact force exerted on the rod by the well is positive for unbuckled and sinusoidally buckled systems. Whenever we measure a negative vertical component, we can then conclude that a somewhat helical buckling has occurred. The results for the cases considered, presented in Fig. 18, show some examples of possible scenarios with sinusoidal or partially/fully helical buckling.

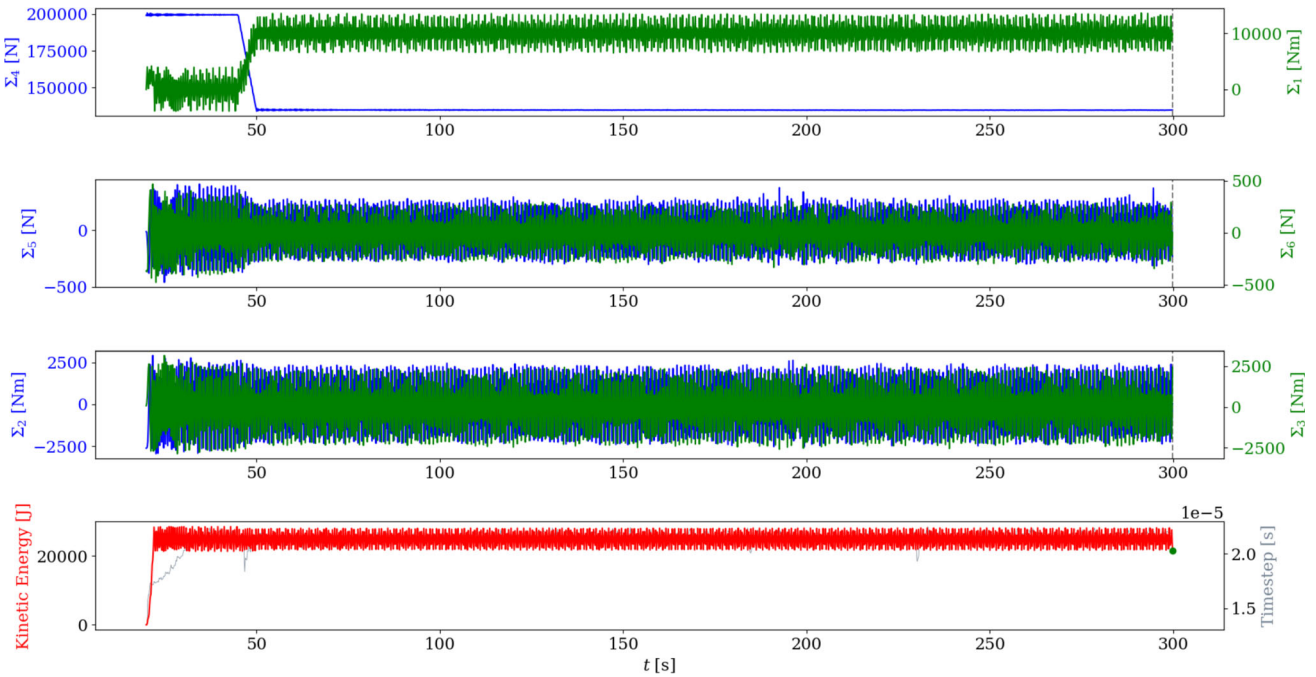

Fig. 21 The numerical simulation for the dynamics of a rod with material parameters given in Table 4 inserted inside the well identified as *Well 1* (with profile given in Fig. 19). After giving the rod a relaxation time of 20 s, an axial rotational speed is imposed at the head; at a time $t = 45$ s, a compressive load is applied at the bit, together with a positive axial momentum (with regime values reached in 5 s). The time evolution of the component of the stresses associated with stretching Σ_4 and twisting Σ_1 (first panel) numerically simulated reproduces the trend of the signal for the corresponding quantities measured in drilling operations (cf. Figure 20)

Table 4 Material parameters of the rod and the well for the numerical simulations presented in Sect. 4.1

Rod	
Parameter	**Value**
Total relaxed length	515 m
Inner diameter	0.2266 m
Outer diameter	0.2445 m
Linear mass density	52.0925 kg/m
Young modulus	200 GPa
Poisson ratio	0
Well	
Parameter	**Value**
Length	520 m
Diameter	0.3111 m
Fluid density	1917 kg/m^3

4 Simulations of the dynamics in realistic geometries

To test the computational efficiency and assess the predictive potentiality of the method we developed, we present now a series of numerical studies for the dynamics of various drill-string systems in realistic geometries. We performed simulations which reproduce drilling conditions, accounting for tortuous shapes of the wells and analysing dynamic solutions obtained by imposing a prescribed rotational speed at the top. The method allows a straightforward analysis of the stress distribution and evolution, and consequently a comparison against significant measurable on-field quantities, which facilitates the identification of safe operating conditions during drilling operations. The data for the geometry of realistic wells and the material parameters of physical rods were provided by Tenaris, together with data collected in on-field measurements. The computational model was implemented in the Python language and all the simulations were run on a Intel® Xeon®W processor at 3.90 GHz with 1 TB disc capacity and 64-bit Ubuntu 20.

4.1 Real data evidence

To validate the reliability of our method in reproducing the mechanical response of real drill-string systems, we tested our numerical simulations of the nonlinear dynamics of constrained rods against measurements collected in drilling operations. Specifically, we compared the profiles of the stresses registered at the top-drive with those predicted by our numerical method, for a rod with material parameters

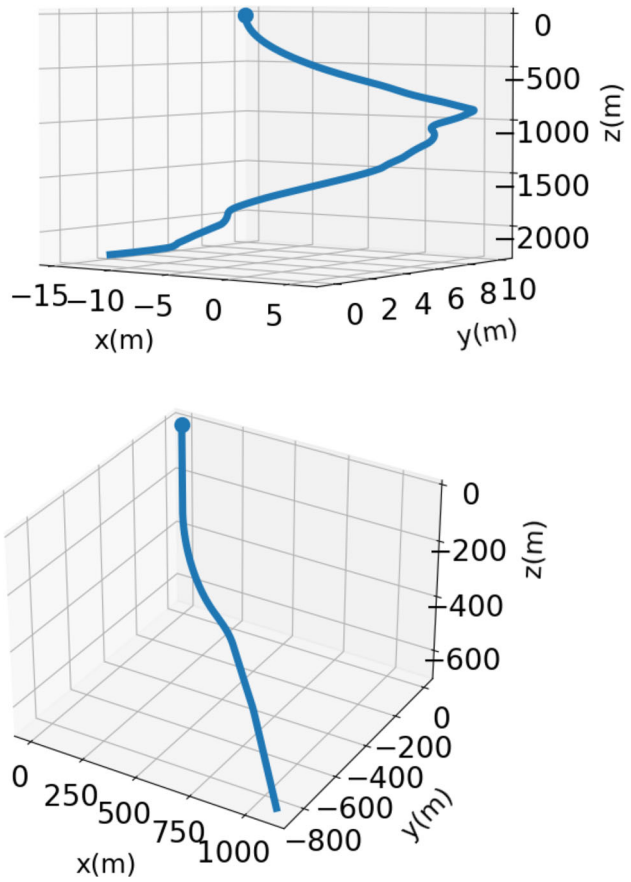

Fig. 22 Three-dimensional representation of the profile of the wells identified as *Well 2* (top) and *Well 3* (bottom). Note that both wells present one or more doglegs, and that while the profile of the former is almost vertical, the latter has a very long almost-horizontal component

given in Table 4, confined inside a well which will be identified by the name *Well 1* (see, in Fig. 19, the well profile).

The representative data set chosen for our test is reported in Fig. 20. The picture shows the temporal evolution of the stresses associated with stretching and twisting, registered at the top-drive of the drill-string system, when a rotational speed of 1.83 Hz is imposed at the head. From the data, it emerges in particular that, during the drilling process, to the presence of a weight on bit (associated with a drop in tension, coloured in blue) corresponds an increase in torque measured at the head (in green). This trend indicates that the contacts between the bit of the drill-string and the bottom of the well are the predominant source of dissipation in the process.

For the numerical simulations, we set the following parameters. The spatial discretisation was performed on a uniform grid with $N = 86$ segments. Internal dissipation was included by assigning the matrix $\mathbb{D}_{\text{in}} = \eta_{\text{in}}\text{diag}(1, 1, 1, 1, 1, 1)$, with damping coefficient $\eta_{\text{in}} = 10^{-2}$ N s/m. The constraint was attained via viscoelastic springs with coefficients $k_{\text{el}} = 10^4$ Pa and $\eta_{\text{el}} = 10^4$ Pa s, while the value $k_{\text{tan}} = 0.5 \cdot 10^4$ Pa was chosen for the tangential springs, together with the friction coefficients $\eta_{0,\text{l}} = \eta_{0,\text{t}} = 0.6$ and $\eta_{\text{dy,l}} = \eta_{\text{dy,t}} = 0.42$. The value of the viscosity of the fluid was fixed to 10^{-3} Pa s.

The set up for the simulation mimicked the operating procedure, as, first, initialising the system with the rod at rest and coaxial with the well, we let the rod relax toward the equilibrium configuration, which was approached within 20 s, following the dissipative dynamics; then, we imposed at the head an angular momentum with frequency 1.83 Hz along the vertical axis (linearly increasing up to regime speed in 2 s); last, to simulate the contact with the bottom of the borehole and the drilling operation, we applied at the bit a compressive load of magnitude 65 kN and a torque opposite to the top-drive of magnitude 10^4 N m (proportionally increasing up to the final values in 5 s). The steady rotational motion was recorded for a time interval of some minutes.

The results are presented in Fig. 21: the first three panels display the time evolution, subsequent to the relaxation, of the six components of the generalised stress at the head of the rod (from top to bottom: stretching and twisting, shearings, bendings), while the bottom panel shows the evolution of the kinetic energy and adaptive time step. The simulation indicates that the contact interaction with the well interests almost exclusively the bit of the rod, as to be expected being the well almost vertical. The temporal profiles of the stresses at the head reveal that our method captures the most significant features emerging from the field measurements. Indeed, the profile of the time evolution of the stresses associated with stretching and twisting emerging from the experimental data (Fig. 20) is satisfactorily reproduced by the numerical solution (top panel in Fig. 21). The proportionality factor between torque and load, which, for the data set considered here, amounts to 0.16 m, allows to estimate the friction coefficient, using (15), which is $\mu_{\text{b}} = 1.6$.

4.2 Computationally-challenging simulations

We finally put to the test the numerical capacity of our method by simulating the dynamics of very long rods, forced at high rotational speeds and confined inside tortuous wells.

We considered two realistic setups, characterised by representative values of drilling systems, which in the following will be identified by the names *Well 2* and *Well 3*, each consisting of a rod, with material parameters variable along its length, constrained by a well with a profile reported in Fig. 22. In the former case, the rod had length $L = 2.254$ km and the spatial discretisation was performed with $N = 322$ segments, while in the latter the corresponding values equaled $L = 1.911$ km and $N = 294$.

In the first test, we simulated the dynamics of the systems in steady rotational motion, obtained by imposing at the head an axial angular momentum with a frequency of 2 Hz. In the second test, together with the top-drive which dictated at the

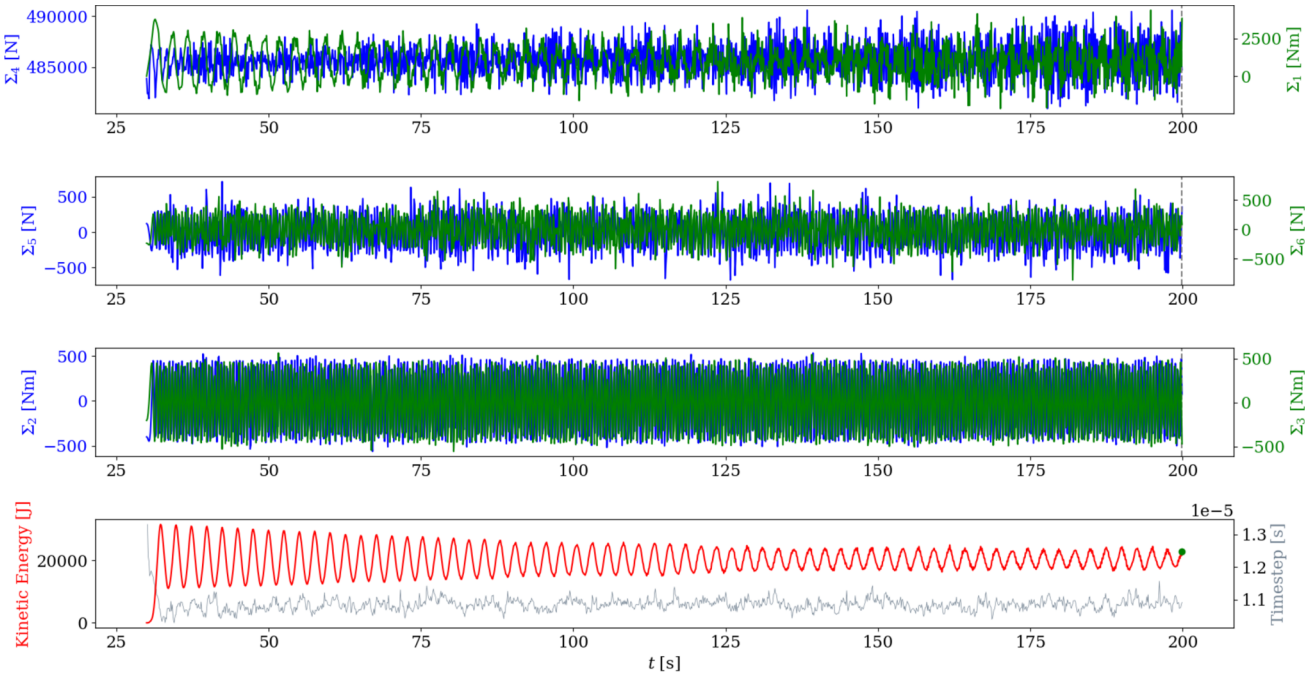

Fig. 23 The numerical simulation for the dynamics of a rod inserted inside the well identified as *Well 2* (with profile given in Fig. 22). The coefficients for the springs are: $k_{\text{el}} = 10^5$ Pa, $\eta_{\text{el}} = 10^5$ Pa s, and $k_{\text{tan}} = 10^3$ Pa. After giving the rod a relaxation time of 30 s, an axial rotational speed is imposed at the head. The time evolution of the components of the generalised stress associated with shearing, Σ_5 and Σ_6, and bending, Σ_2 and Σ_3, undergo quasiperiodic motions, with zero-mean values; on the other hand, those associated with stretching, Σ_4, and twisting, Σ_1, display oscillatory motions around a mean value different from the equilibrium one, consequent to contact interactions. The simulation is stable for the time window considered (200 s) and the adaptive stepsize stabilises around 10^{-5} s

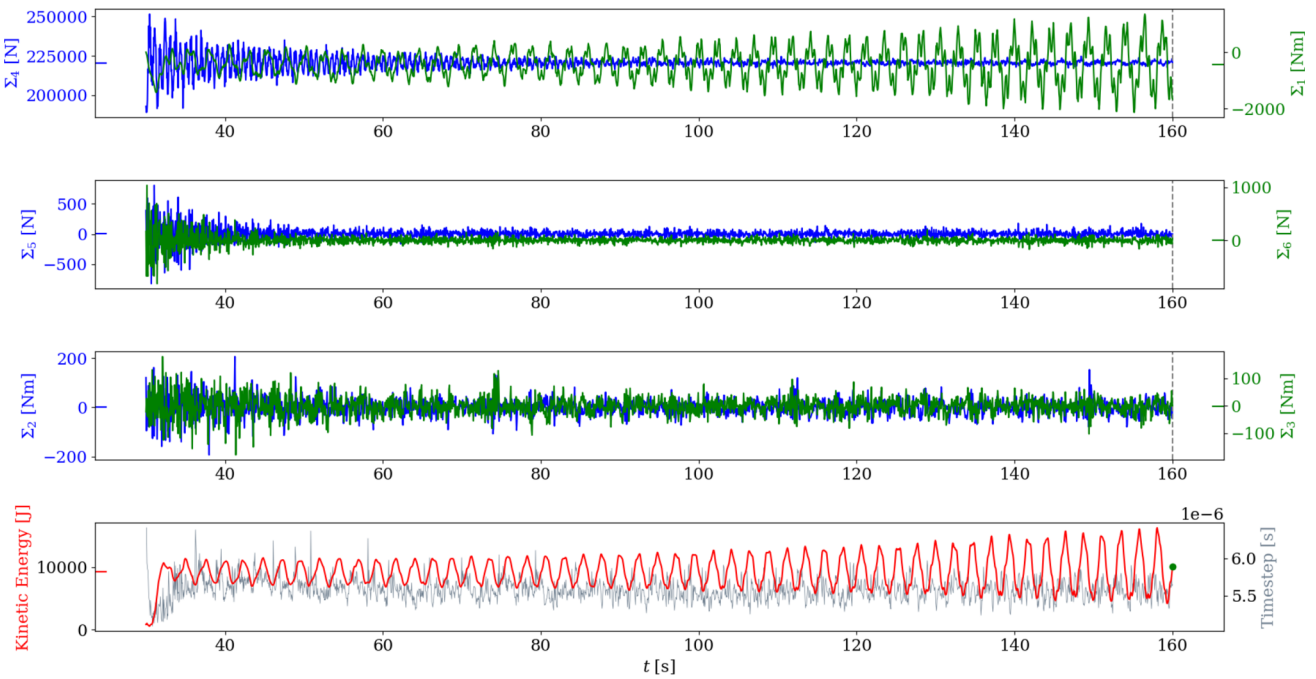

Fig. 24 The numerical simulation for the dynamics of a rod inserted inside the well identified as *Well 3* (with profile given in Fig. 22). The coefficients for the springs are: $k_{\text{el}} = 10^6$ Pa, $\eta_{\text{el}} = 10^6$ Pa s, and $k_{\text{tan}} = 10$ Pa. After giving the rod a relaxation time of 30 s, an axial rotational speed is imposed at the head. The time evolution of the generalised stresses at the head reflects the significant impact on the dynamics of the rod of the long horizontal part of well, which produces extended contact interactions. The oscillation amplitudes of the component of the stresses associated with stretching, Σ_4, shearing, Σ_5 and Σ_6, and bending, Σ_2 and Σ_3, decay to zero, whereas the component associated with twisting, Σ_1, displays a more complicated dynamics with modulated oscillations, increasing in amplitudes and with meanvalue significantly lower than zero. The simulation is stable for the time window considered (160 s) and the adaptive stepsize stabilises above $0.5 \cdot 10^{-5}$ s

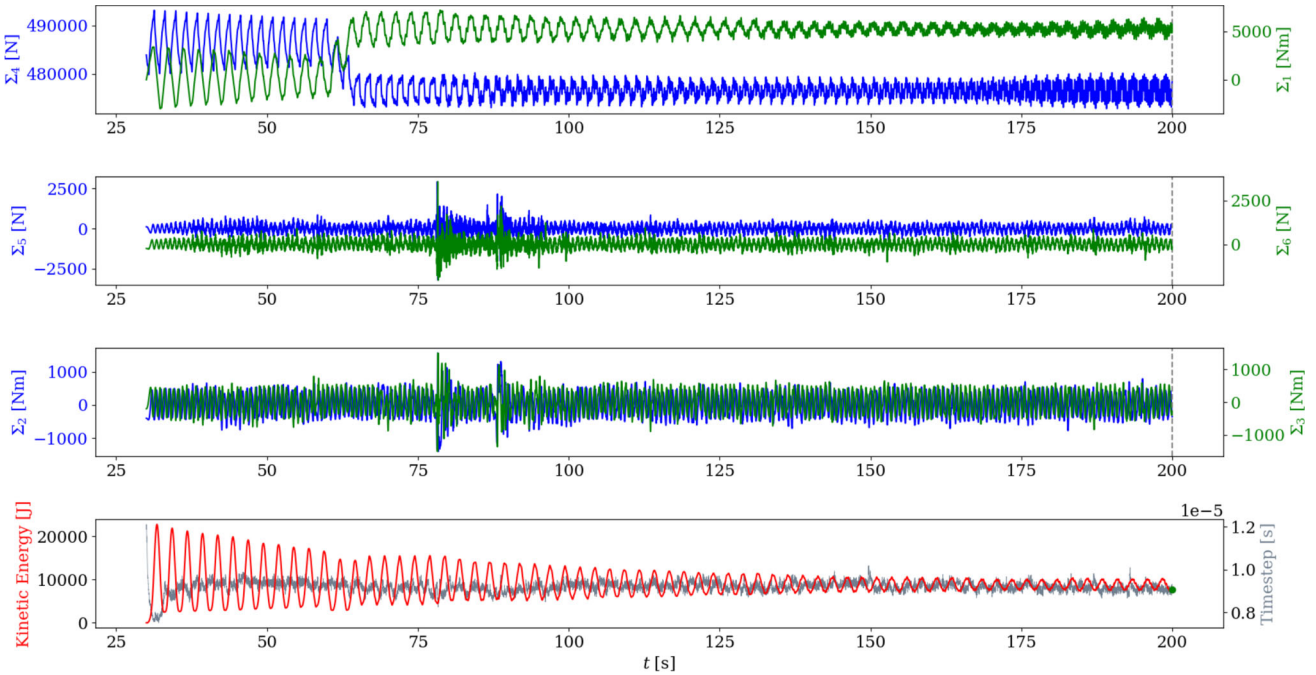

Fig. 25 The numerical simulation for the dynamics of a rod inserted inside the well identified as *Well 2* (with profile given in Fig. 22). The coefficients for the springs are: $k_{\text{el}} = 10^6$ Pa, $\eta_{\text{el}} = 10^6$ Pa s, and $k_{\text{tan}} = 10$ Pa. After giving the rod a relaxation time of 30 s, an axial rotational speed is imposed at the head of the rod and, at a time $t = 60$ s, a compressive load and a torque are applied at the bit. The time evolution of the component of the generalised stresses associated with stretching, Σ_4, and twisting, Σ_1, is characterised by modulated oscillations, while those associated with bending, Σ_2 and Σ_3, and shearing, Σ_5 and Σ_6, display quasiperiodic motions, with the exception of two consecutive localised spikes. These events, likely due to stick–slip phenomena, indicate that the method captures the details of abrupt changes in the values of the stresses without numerical instabilities. The simulation is in fact stable for the whole time window considered (200 s) and the adaptive stepsize stabilises around $0.9 \cdot 10^{-5}$ s

head a rotational speed with a frequency of 0.3 Hz, at the bit it was applied a compressive load of magnitude 10 kN and a vertical torque of magnitude equal to 5 kN m.

For the numerical simulations, we set the following parameters. Internal dissipation was included by assigning the matrix $\mathbb{D}_{\text{in}} = \eta_{\text{in}}\text{diag}(1, 1, 1, 1, 1, 1)$, with damping coefficient $\eta_{\text{in}} = 10^{-2}$ N s/m, while the friction coefficients were $\eta_{0,\text{l}} = \eta_{0,\text{t}} = 0.6$ and $\eta_{\text{dy,l}} = \eta_{\text{dy,t}} = 0.42$. The value of the viscosity of the fluid was $\mu = 10^{-2}$ Pa s. Regarding the spring constants for the normal and tangential elastic response, the combination of larger sizes of the rod, more curved well geometries, and loads at the drilling bit requires a more careful calibration of the model parameters. Larger values of the normal spring coefficients k_{el} are necessary to avoid excessive interpenetration. On the other hand, increasing the tangential coefficient k_{tan} in the same way can lead to constraints on the time step that would make the simulation impractical. With the current contact model, we were able to achieve reasonable simulations by setting k_{tan} at values that are somewhat smaller than what is usually advisable. The specific values chosen for each simulation are indicated in the captions of the corresponding figures. As we mention in the Conclusions, there is room for improving the contact model, with an impact on the calibration of parameters as well.

All the numerical simulations that we performed remained stable and the time evolution was computed over several minutes, with an adaptive time step in all cases greater than $0.5 \cdot 10^{-5}$ s.

4.2.1 Steady rotational regime

We simulated the dynamics of two nonhomogeneous and very long rods in a steady rotational motion along the longitudinal axis, obtained by imposing at the head an axial angular momentum with a frequency of 2 Hz. The results are presented in Fig. 23 for the well *Well 2*, and Fig. 24 for the well *Well 3*.

The profiles of the time evolution of the stresses at the head that were obtained reflect, on the one hand, the significant length of the rods (causing delayed propagation of signals), on the other, the geometries of the two wells (*Well 3* presents a horizontal deflection, hence contact interactions are especially relevant). In *Well 2*, the components of the stresses associated with the two bendings and shearings display quasiperiodic dynamics, with zero-mean, while the

stretching and the twist, after a transient, oscillate about a mean value which is, respectively, slightly above/below the equilibrium one. In *Well 3*, the mean of the twisting component is even more shifted: the offset, residual of the imposed torque, can be attributed to the contacts with the well, which are greater for the second well, given its long horizontal part; same for the stretching, which, after a transient characterised by large oscillations, stabilises about a mean value above its equilibrium. For both wells, the energy of the system in steady rotational motion transfers predominantly to the bending and twisting components.

4.2.2 Drilling operation

Finally, we present the results obtained for the well identified as *Well 2*, when a rotational speed of 0.3 Hz is imposed at the head of the rod, together with both a compressive load (of magnitude 10 kN) and a torque (of magnitude 5 kN m) applied at the bit. The results of the numerical simulation are shown in Fig. 25.

5 Conclusions

We proposed a method for the simulation of drill-string systems with fluid–structure and contact interactions in realistic geometries.

We adopted, for the modelling of the drill-string as a slender viscoelastic structure, the method developed by [31], which we tested in simulations of buckling phenomena. The drill-string is viewed as a viscoelastic Cosserat rod confined inside cylindrical wells filled with fluid. The dynamics is given in terms of generalised momenta and stresses, elements of the special Euclidean algebra, and contact and fluid–structure interactions are implemented as external dissipative generalised forces. We implemented the approximation scheme for the spatial discretisation using finite differences on a staggered grid and for the temporal integration the explicit RKDP method with adaptive time-stepping. We accounted for the hydrodynamical dissipation introduced by the interaction with drilling fluids by modelling the rod as a translating–rotating mixer moving in an incompressible viscous Newtonian fluid in the slow-flow approximation. The model permits to describe contributions which are sensitive not only to the velocity of the rod, but also to its location within the well, in a numerically efficient way by adjusting the viscosity coefficients. We modelled the contact interactions with the well via radial viscoelastic springs, and tangential springs with storing and sliding regimes. The contact model that we employ is a penalisation method. As such, contact forces only arise in the presence of a nonzero penetration of the beam inside the solid walls, which is of course unphysical. We consider a small penetration to be acceptable in view of the uncertainty about the real roughness of the wall. In practice, one can calibrate the normal stiffness of the constraint to remain below a given penetration threshold. The penetration that we observe in Fig. 16c is below 35 mm, but is strongly emphasised by the radial zoom on the rendering. We stress that this value is a bit large but it originates from the very strong force that we apply in this example to show the different buckling regimes. In the realistic applications the penetration remains below a few millimeters. The choice of an adaptive time-stepping is also helpful in avoiding excessive penetration. In the present work, we do not take into account the deformability of either the drilling pipe or the surrounding ground. A possible direction for further improvement of the contact treatment may be to employ nonlinear models such as the Hertzian one. We included, as input data on the boundary conditions, a bit-rock interaction described as an axial torque linear in the applied compressive load, produced by Coulomb friction on a rotating spherically-shaped bit. The latter contribution is the most significant dissipative source and its effect is visible in on-field measurements.

We tested our method in static and dynamic regimes, for realistic values of the material parameters and realistic geometries. The results of our numerical simulations showed a very good agreement with measurements collected in drilling operations, as the profiles of the signals registered at the head were satisfactorily reproduced by time evolution of the simulated stresses. Moreover, when tested in computationally-challenging configurations, such as long rods and tortuous wells, the method proved to be stable and capable of reproducing details of the nonlinear dynamics of the drill-string which are useful in preventing fractures of the pipes during drilling operations.

Funding This study was funded by Tenaris.

Declarations

Conflict of interest The authors have no relevant financial or non-financial interests to disclose.

References

1. Johancsik CA, Friesen DB, Dawson R (1984) Torque and drag in directional wells-prediction and measurement. J Petrol Technol 36:987–992. https://doi.org/10.2118/11380-PA
2. Locke HA, Johnson JB, Jewkes DC (1988) Extended reach appraisal well: A case history. In: SPE International Oil and Gas Conference and Exhibition in China, SPE-17564-MS, https://doi.org/10.2118/17564-MS
3. Maidla EE, Wojtanowicz AK (1987) Field comparison of 2-d and 3-d methods for the borehole friction evaluation in directional wells. In: SPE Annual Technical Conference and Exhibition, SPE-16663-MS, https://doi.org/10.2118/16663-MS
4. Baker R (2001) A Primer of Oilwell Drilling: A Basic Text of Oil and Gas Drilling, 6th edn. Petroleum Extension Service, Continuing & Extended Education, University of Texas at Austin, Austin, Texas
5. Macdonald KA, Bjune JV (2007) Failure analysis of drillstrings. Eng Fail Anal 14(8):1641–1666. https://doi.org/10.1016/j.engfailanal.2006.11.073
6. Albdiry M, Almensory M (2016) Failure analysis of drillstring in petroleum industry: a review. Eng Fail Anal 65:74–85. https://doi.org/10.1016/j.engfailanal.2016.03.014
7. Mitchell R, Samuel R (2009) How good is the torque-drag model? SPE Drill Compl 24:62–71. https://doi.org/10.2118/105068-PA
8. Maidla EE, Wojtanowicz AK (1988) A field method for assessing borehole friction for directional well casing. J Petrol Sci Eng 1(4):323–333. https://doi.org/10.1016/0920-4105(88)90007-1
9. Samuel R (2010) Friction factors: what are they for torque, drag, vibration, bottom hole assembly and transient surge/swab analyses? J Petrol Sci Eng 73(3):258–266. https://doi.org/10.1016/j.petrol.2010.07.007
10. Mirhaj SA, Kaarstad E, Aadnoy BS (2016) Torque and drag modeling; soft-string versus stiff-string models. In: SPE/IADC Middle East Drilling Technology Conference and Exhibition, D033S012R003, https://doi.org/10.2118/178197-MS
11. Chen SL, Blackwood K, Lamine E (2002) Field investigation of the effects of stick-slip, lateral, and whirl vibrations on roller-cone bit performance. SPE Drill Complet 17(01):10–15. https://doi.org/10.2118/76811-PA
12. Spanos PD, Chevallier AM, Politis NP et al (2003) Oil and gas well drilling: a vibrations perspective. Shock Vib Digest 35:85–103. https://doi.org/10.1177/0583102403035002564
13. Kapitaniak M, Hamaneh VV, Wiercigroch M (2016) Torsional vibrations of helically buckled drill-strings: experiments and fe modelling. J Phys: Conf Ser 721(1):012012. https://doi.org/10.1088/1742-6596/721/1/012012
14. Khulief YA, Al-Sulaiman FA, Bashmal S (2007) Vibration analysis of drillstrings with self-excited stick-slip oscillations. J Sound Vib 299(3):540–558. https://doi.org/10.1016/j.jsv.2006.06.065
15. Tran QT, Nguyen KL, Manin L et al (2019) Nonlinear dynamics of directional drilling with fluid and borehole interactions. J Sound Vib 462:114924. https://doi.org/10.1016/j.jsv.2019.114924
16. Arbatani S, Callejo A, Kövecses J et al (2016) An approach to directional drilling simulation: finite element and finite segment methods with contact. Comput Mech 57:1001–1015. https://doi.org/10.1007/s00466-016-1274-2
17. Nguyen KL, Mahjoub M, Tran QT, et al (2020) Nonlinear dynamics of a drillstring immersed in a 3d curved well, simulations and experiments. In: SPE/IADC Drilling Conference and Exhibition, D082S000R004, https://doi.org/10.2118/199675-MS
18. Hakimi H, Moradi S (2010) Drillstring vibration analysis using differential quadrature method. J Petrol Sci Eng 70(3):235–242. https://doi.org/10.1016/j.petrol.2009.11.016
19. Moharrami M, de Arruda Martins C, Shiri H (2021) Nonlinear integrated dynamic analysis of drill strings under stick-slip vibration. Appl Ocean Res 108:102521. https://doi.org/10.1016/j.apor.2020.102521
20. Yuan H, Dong G, Chen Y et al (2022) The vibration modal characteristics of drillstring in compound drilling. J Phys: Conf Ser 2208:012006. https://doi.org/10.1088/1742-6596/2208/1/012006
21. Auriol J, Kazemi N, Niculescu SI (2021) Sensing and computational frameworks for improving drill-string dynamics estimation. Mech Syst Signal Process 160:107836. https://doi.org/10.1016/j.ymssp.2021.107836
22. Liu Y, Chávez J, Sa R et al (2017) Numerical and experimental studies of stick-slip oscillations in drill-strings. Nonlinear Dyn 90:2959–2978. https://doi.org/10.1007/s11071-017-3855-9
23. Tian J, Wu C, Yang L et al (2016) Mathematical modeling and analysis of drill string longitudinal vibration with lateral inertia effect. Shock Vib 2016:1–8. https://doi.org/10.1155/2016/6281264
24. Germay C, Wouw N, Nijmeijer H et al (2009) Nonlinear drillstring dynamics analysis. SIAM J Appl Dyn Syst 8:527–553. https://doi.org/10.1137/060675848
25. Ritto TG, Soize C, Sampaio R (2010) Robust optimization of the rate of penetration of a drill-string using a stochastic nonlinear dynamical model. Comput Mech 45(5):415–427. https://doi.org/10.1007/s00466-009-0462-8
26. Trindade M, Wolter C, Sampaio R (2005) Karhunen-loève decomposition of coupled axial/bending vibrations of beams subject to impacts. J Sound Vib 279(3):1015–1036. https://doi.org/10.1016/j.jsv.2003.11.057
27. Yigit AS, Christoforou AP (1998) Coupled torsional and bending vibrations of drillstrings subject to impact with friction. J Sound Vib 215:167–181. https://doi.org/10.1006/jsvi.1998.1617
28. Christoforou A, Yigit A (2003) Fully coupled vibrations of actively controlled drillstrings. J Sound Vib 267(5):1029–1045. https://doi.org/10.1016/S0022-460X(03)00359-6
29. Cunha A Jr, Soize C (2015) Computational modeling of the nonlinear stochastic dynamics of horizontal drillstrings. Comput Mech 56(5):849–878. https://doi.org/10.1007/s00466-015-1206-6
30. Mohammadzadeh M, Shahgholi M, Arbabtafti M et al (2020) Vibration analysis of the fully coupled nonlinear finite element model of composite drill strings. Arch Appl Mech 90:1373–1398. https://doi.org/10.1007/s00419-020-01673-8
31. Giusteri GG, Miglio E, Parolini N et al (2022) Simulation of viscoelastic cosserat rods based on the geometrically exact dynamics of special euclidean strands. Int J Numer Meth Eng 123(2):396–410. https://doi.org/10.1002/nme.6860
32. Finn M, Cox S (2001) Stokes flow in a mixer with changing geometry. J Eng Math 41:75–99. https://doi.org/10.1023/A:1011840630170
33. Kruse R, Nguyen-Thanh N, De Lorenzis L et al (2015) Isogeometric collocation for large deformation elasticity and frictional contact problems. Comput Methods Appl Mech Eng 296:73–112. https://doi.org/10.1016/j.cma.2015.07.022
34. Marino E (2017) Locking-free isogeometric collocation formulation for three-dimensional geometrically exact shear-deformable beams with arbitrary initial curvature. Comput Methods Appl Mech Eng 324:546–572. https://doi.org/10.1016/j.cma.2017.06.031
35. Ignesti D, Ferri G, Auricchio F et al (2023) An improved isogeometric collocation formulation for spatial multi-patch shear-deformable beams with arbitrary initial curvature. Comput Methods Appl Mech Eng 403:115722. https://doi.org/10.1016/j.cma.2022.115722

36. Dormand J, Prince P (1980) A family of embedded runge-kutta formulae. J Comput Appl Math 6(1):19–26. https://doi.org/10.1016/0771-050X(80)90013-3
37. Joseph DD, Munson BR (1970) Global stability of spiral flow. J Fluid Mech 43(3):545–575. https://doi.org/10.1017/S0022112070002574